Check for updates

Induced seismicity associated with geothermal fluids re-injection: Poroelastic stressing, thermoelastic stressing, or transient cooling-induced permeability enhancement?

Wenzhuo Cao [a,*], Sevket Durucan [a], Ji-Quan Shi [a], Wu Cai [a,b], Anna Korre [a], Thomas Ratouis [c]

[a] Department of Earth Science and Engineering, Royal School of Mines, Imperial College London, London, United Kingdom
[b] State Key Laboratory of Coal Resources and Safe Mining, China University of Mining and Technology, Xuzhou, Jiangsu 221116, China
[c] Orkuveita Reykjavíkur, Bæjarhálsi 1, 110 Reykjavik, Iceland

ARTICLE INFO

ABSTRACT

Both field injectivity and induced seismicity were reported to be inversely correlated with the temperature of re-injected fluids at the Hellisheiði geothermal field in Iceland. This observation has led to a hypothesis that transient cooling-induced permeability enhancement is a novel mechanism for induced seismicity, in addition to elevated fluid pressure, poroelastic stressing, and thermoelastic stressing in geothermal environments. In this work, a 3D calibrated coupled THM model was developed to model the colder fluids re-injection process over a 1-year period and evaluate the potential for induced seismicity in terms of Coulomb stress changes at the Hellisheiði geothermal field. Three modelling scenarios taking into account respectively the poroelastic effect, thermoporoelastic effect, and thermoporoelastic effect with permeability enhancement, were examined and compared to identify the dominant mechanism for the recorded seismicity and examine the contribution from each individual mechanism. Results have shown that, under normal fluid re-injection pressure and temperature conditions, the permeability enhancement effect is the dominant mechanism for induced seismicity at the Hellisheiði geothermal field. Specifically, the contribution to Coulomb stress changes from the permeability enhancement effect is almost twice of that from the thermoelastic stressing, which is in turn two orders of magnitude larger than that from the poroelastic stressing. It has also been noted that, when reducing temperature of re-injected fluids from 120°C to 20°C, the temperature change is increased by 2.1 times at 1,000 m depth, while the amount of mass flow by around 4 times. Thus, the amount of heat transferred can be increased 8.4 times by lowering temperature of the injected fluids, which explains the high sensitivity of induced seismicity to temperature. Outcomes of this work suggest temperature control of injected fluids as a feasible regulation method to mitigate against injection-induced seismic risk in geothermal reservoirs.

1. Introduction

Induced seismicity has long been a major challenge faced by the geothermal industry, amongst other industries concerned with fluid injection into or resources extraction from the subsurface, such as carbon storage (e.g., Rutqvist et al., 2016), wastewater injection (e.g., Weingarten et al., 2015), hydraulic fracturing (e.g., Schultz et al., 2020), and underground mining (e.g., Si et al., 2020). Observations at 64 enhanced geothermal systems (EGS) sites have shown that induced seismicity has impacted most EGS sites and caused the termination or cessation of operations 6 or more sites worldwide (Pollack et al., 2020). The most striking example of geothermal exploitation-related induced

seismicity is the Pohang M_w 5.5 earthquake in 2017, which was the most damaging earthquake experienced in Korea for centuries (Grigoli et al., 2018). Experience in the hydrothermal usage of a deep natural aquifer in the North Alpine Foreland Basin has shown that non-pressure-stimulated geothermal fields could also generate shallow earthquakes at low injection pressures in low seismic hazard settings (Megies and Wassermann, 2014). In addition to adverse physical effects on buildings and facilities in the surrounding communities, the magnitude and intensity of injection-induced seismicity associated with current and future geothermal exploitation remain a great public concern.

Deep geothermal systems, either hydrothermal or enhanced geothermal systems, exploit heat from subsurface hot rocks in a

---

continuous cycle by pumping spent fluids or fresh water into injection wells, and extracting thermal fluids from production wells several kilometres away. Typical mechanisms identified for induced seismicity in geothermal environments include fluid pore pressure increase, poroelastic stressing, thermoelastic stressing, and chemical alteration of frictional properties of fractures (Majer et al., 2007; Rathnaweera et al., 2020). Experimental investigations on fracture shear slippage subjected to fluid injection (e.g., Ji et al., 2022; Ji and Wu, 2020; Ye and Ghassemi, 2018), thermal effects (Sun et al., 2021) and chemical reactions (Fuchs et al., 2021) have contributed significantly towards the understanding of the mechanisms of induced seismicity. As a specific mechanism relevant to geothermal systems, the thermoelastic effect has been of particular research interest in recent years. Water and steam production takes heat away from geothermal reservoirs, causing modest temperature drawdown around production wells (Segall and Fitzgerald, 1998). On the other hand, water injected into subsurface reservoirs is much colder than hot rocks, producing a remarkable temperature contrast in the neighbourhood of injection wells (Jeanne et al., 2014a). The resultant thermoelastic stress change, analogous to the poroelastic stress change, influences the occurrence of induced seismicity by changing the prevailing stress states.

The distinctions in physical processes of fluid flow and heat transfer and the associated intrinsic hydrological and thermodynamic parameters determine that hydraulic and thermoelastic effects exert different influences on induced seismic characteristics (intensity, location, and timing). While seismicity occurrence is under the compound effects of these mechanisms, the extent to which seismic intensity is influenced by pore pressure change and thermoelastic stressing varies from site to site, depending on the in-situ stress states and field operational conditions (injection pressure and temperature of injected fluids). For example, the key mechanism relevant to seismic event count and seismic moment has been the injection-induced pressure increase at the Newberry EGS field (Izadi and Elsworth, 2015). In contrast, it is likely that thermoelastic stressing is the dominant effect in triggering induced seismicity at some other geothermal fields, such as the Geysers field (Segall and Fitzgerald, 1998). Extensive analytical and modelling investigations have also been performed to unravel the relative contribution from the two effects. Analytical analysis of the role of thermo-poro-elastic stresses on induced seismicity around an individual fracture supported that thermoelastic stressing is the dominant mechanism, which could cause the seismicity rate to rise by over 1,000-fold within 200 m distance from the fracture (Candela et al., 2018). Comparison between thermo-hydro-mechanical (THM) and hydro-mechanical (TM) modelling also showed that thermoleastic effect prevails over hydraulic effect in triggering induced seismicity when the maximum principal stress is oriented perpendicular to fractures (De Simone et al., 2013).

As fluid flows are much faster than heat transfer in fractured reservoir rocks, the thermal front lags behind the hydrodynamic front emanating from injection wells (Izadi and Elsworth, 2015). This brings about appreciable distinction between induced seismicity relevant to the hydraulic and thermoelastic effects in terms of spatial distribution and temporal evolution features. Induced seismicity was believed to be primarily caused by thermal drawdown near injection wells where transient cooling prevails, and by elevated pore pressure away from injection wells at the Geysers geothermal field (Jeanne et al., 2014b). Induced seismicity is initiated as a result of hydraulic effects shortly after the onset of fluid injection (in days to months), and thermoelastic effect over longer periods of time (in months to years) (Izadi and Elsworth, 2015). In addition, the time sequence of the hydraulic and thermoelastic effects affects the injection fluid pressure in reservoirs, which initially increases due to the poroelastic stressing, followed by reduction in response to the thermoelastic stressing over time (Ghassemi and Tao, 2016).

In addition to the direct thermoelastic stressing discussed above, examination of the full coupling multiphysics reveals that thermal effects have strong control on both the hydrological and thermodynamic behaviour through first thermo-mechanical coupling, then mechanical-hydro coupling, and finally hydro-thermo coupling. Thermal drawdown caused by cold water injection causes the contraction of rock matrix and corresponding increase of fracture aperture, which in turn increase the permeability of reservoir rocks. As a result, diffusion of pore pressure and changes in stress states take place, and the thermoelastic effect itself is also further enhanced as driven by the intensified fluid flow. The coupling between the three physical processes iterates until an equilibrium is reached for each individual process. This effect, referred to as transient cooling-induced permeability enhancement in this work, was confirmed by field measurements that the injectivity index is inversely correlated with bottomhole temperature at a number of geothermal sites, such as the Los Azufres field in Mexico (Benson, 1987), the Sumikawa field in Japan (Ariki and Hatakeyama, 1997), and the Hellisheiði site in Iceland (Gunnarsson, 2013). Similar temperature-dependent injectivity behaviour has also been broadly noticed when cold CO_2 is injected into subsurface at various sites (Lee et al., 2009), including the In Salah site in Algeria (Vilarrasa et al., 2017), the Sleipner site in Norway (Hodneland et al., 2019), and the Aquistore (Rangriz Shokri et al., 2019) and Quest (Tawiah et al., 2020) sites in Canada.

Over the past decades, extensive numerical analyses have been conducted to investigate the coupled THM behaviour (Ghassemi and Zhou, 2011; Koh et al., 2011; Zhou et al., 2009), heat production performance (Parisio et al., 2019; Yao et al., 2018), permeability evolution (Ghassemi et al., 2008; Ghassemi and Kumar, 2007; Kang et al., 2022; Pandey et al., 2017) and induced seismicity (Blöcher et al., 2018; Candela et al., 2018; De Simone et al., 2013; Eyinla and Oladunjoye, 2021; Gan and Elsworth, 2014a, 2014b; Gan and Lei, 2020; Safari and Ghassemi, 2015) in geothermal systems. However, to the best knowledge of the authors, the effect of transient cooling-induced permeability enhancement on stress changes in relation to induced seismic occurrence has not been reported in the literature. It is believed by the authors that this phenomenon may have a positive effect on induced seismicity by enhancing both fluid flow and heat transfer, as compared to when it is neglected (i.e., solely under the thermoporoelastic effect).

The objectives of the current work were two-fold: 1) to identify the governing mechanism for induced seismicity associated with injection of cold water in geothermal reservoirs; 2) to examine to which extent induced seismicity associated with geothermal exploitation is dependent on the temperature. To this end, a coupled thermal-hydro-mechanical (THM) model with stress-dependent permeability was constructed to simulate geothermal fluids injection, and evaluate the potential for induced seismicity under various temperatures using the Hellisheiði geothermal field as a case study. To isolate the contribution from each individual mechanism, the potential for induced seismicity was evaluated in three modelling scenarios, i.e., under poroelastic effect, under thermoporoelastic effect, and under thermoporoelastic effect with permeability enhancement, respectively. Model results were compared against field injectivity measurements at various temperatures and locations of induced seismicity recorded.

2. Temperature-dependent injectivity and induced seismicity at Hellisheiði

Located in the south of the Hengill Volcanic System, SW-Iceland, the Hellisheiði geothermal field is one of the largest geothermal fields in the country. The geothermal field supplies the Hellisheiði heat and power plant which was commissioned in 2006 and has been operated by Orkuveita Reykjavíkur (Reykjavik Energy). The power plant produces electricity and hot water using water-steam mixture at $240 - 320°C$ from a subsurface reservoir at a depth of up to 3.3 km. The total installed capacity of the geothermal plant is 303 MWe for electricity generation and 200 MWth for space heating.

The general stratigraphy in the Hengill area is comprised of alternating successions of hyalocalstic formations formed during glacial
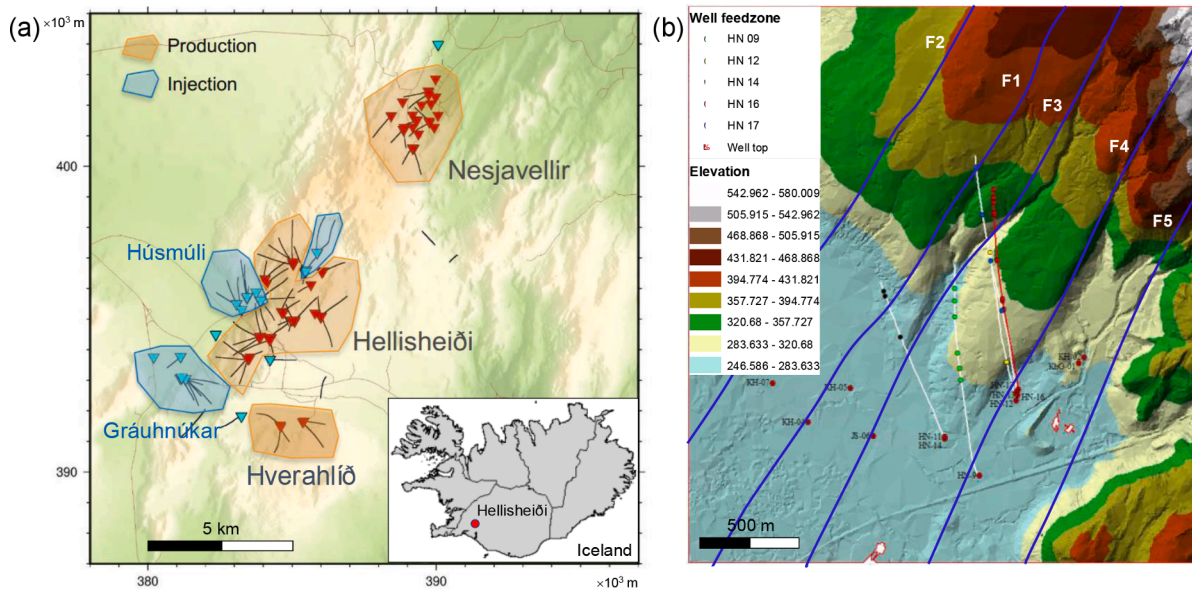
Figure 1. (a) Map of the Hellisheiði geothermal field showing the location of main production and re-injection sites. Coordinates in the map follow the ISN93 geographic coordinate system suitable for use in Iceland. The inset shows the location of Hellisheiði in Iceland. (b) Map of the Húsmúli area showing the location of five geothermal fluid re-injection wells (HN09, HN12, HN14, HN16 and HN17) and five fault structures (F1- F5). The background contours show the elevation of surface topography.
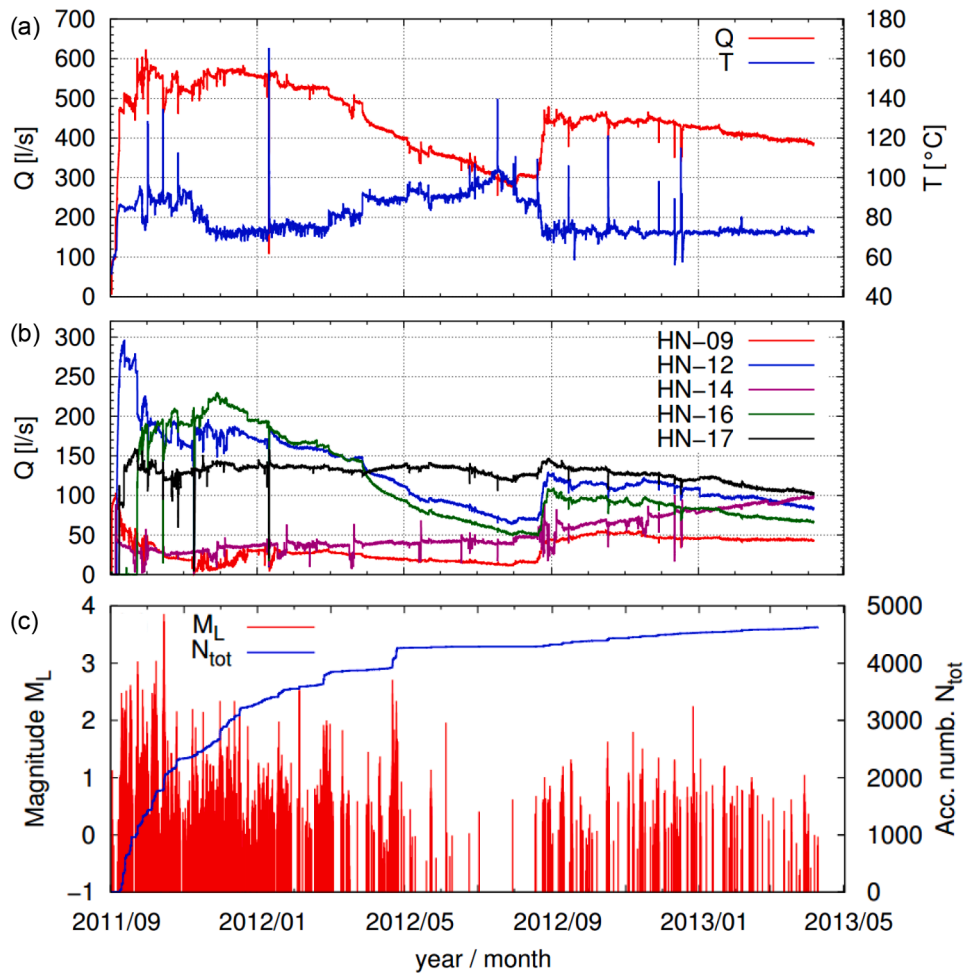
Figure 2. (a) Temperature and total flow rate of injected fluids into the re-injection zone, and (b) injected fluids flow rate into individual injection wells, and (c) seismic magnitude and accumulated event count of induced seismicity during September 2011 – May 2013 at the Húsmúli area (after Gunnarsson, 2013).

periods and lava sequences during interglacial periods. The tectonic setting of the area is characterised by NNE-SSW trending extensional fault structures with sub-vertical dips, as well as highly fractured fissure swarms (Snæbjörnsdóttir et al., 2018). The present-day maximum horizontal principal stress trends to the NNE direction, which is aligned with the strike of local fault structures (Batir, 2011).

Spent fluids from the geothermal plant are re-injected into the subsurface reservoir, following the relevant regulations and operation permits. The re-injection operations of geothermal brine and condensate take place in two sites, the Gráuhnúkar area on the southern edge of the field, and the Húsmúli area on the northern edge (Figure 1a). The Húsmúli area is the main re-injection site with five injection wells (HN09, HN12, HN14, HN16 and HN17) Figure 1.b presents the surface topography of the Húsmúli area with the location of the five wells and five fault structures (F1- F5). Trajectories of the injection wells cut across one or more of the fault structures, and the fluid flow in the geothermal reservoir is controlled by fracture permeability. Wells are cased down to around 800 m depth to avoid loss of circulation fluids (Snæbjörnsdóttir et al., 2018).

Upon commissioning of the Húsmúli re-injection site in September 2011, fluid re-injection first started in four wells (HN09, HN12, HN14 and HN17) on 1 September 2011, and then well HN16 on 23 September (Juncu et al., 2020). The temperature of the re-injected spent fluids mostly fluctuated between 70°C and 100°C, and the wellhead pressure for each individual injection well was maintained at 8 bar during the operations Figure 2. presents the temperature and mass flow rate of the re-injected fluids into the wells during the period from September 2011 to mid-April 2013 at the Húsmúli area. A distinct negative correlation was noted between temperature of re-injected fluids and the amount of re-injected fluids (Figure 2a). The hydrological behaviour of the geothermal reservoir is so sensitive to temperature variations that even a temperature increase of ~30°C caused the total flow rate to fall by almost half, from around 550 l/s to 300 l/s. The high sensitivity of this correlation is also evidenced by the observation that each spike in the temperature curve results in an instantaneous drop in the fluid mass flow rate Gunnarsson et al. (2013). attributed this temperature-dependent injectivity to the rock expansion/contraction in response to thermal shock, which results in a change in fracture aperture and thus hydraulic conductivity of reservoir rocks.

Fluid re-injection into the subsurface reservoir at the Húsmúli area was accompanied with induced seismicity of unprecedently high intensity. As shown in Figure 2c, there is a steep rise in the accumulated seismic event count immediately after the start of re-injections, followed by much modest growth over time. It is noteworthy that induced seismicity almost faded out over the period May – August 2012, when there is an increase in temperature and a corresponding drop in the volume of re-injected fluids (Figure 2c). When the temperature of re-injected fluids fell back to around 70°C in August 2012, the intensity of induced seismicity rose back to the previous levels. These observations suggest that thermal effect, along with hydraulic effect, has a predominant role on seismic occurrence at the Hellisheiði geothermal field.

Thermal effect can influence the occurrence of seismicity in two ways: 1) direct thermoelastic effect, which modifies the prevailing stress field through TM coupling but does not affect the hydrological process in the reservoir; 2) transient heating/cooling-induced permeability change, which influences the prevailing stress field through full THM coupling by changing both hydrological properties and behaviour of the reservoir rocks. To ascertain the dominant mechanism for the induced seismicity, as well as the contribution from each individual mechanism, coupled THM modelling of fluid injection at the Hellisheiði geothermal field was carried out using COMSOL Multiphysics software. A 3D THM model of the geothermal field with stress-dependent permeability was constructed and calibrated against the field injectivity data. The calibrated model was then used to evaluate injection-induced potential for seismicity at the Hellisheiði geothermal field.

3. Governing equations for THM coupling in geothermal exploitation

3.1. Fluid flow in reservoir rocks

Fluid flow through reservoir rocks satisfies the mass conservation equation:

$$\frac{\partial}{\partial t}\left(\rho_f \phi\right) + \nabla\cdot\left(\rho_f \mathbf{v}\right) = Q_f - \rho_f \alpha \frac{\partial \varepsilon_V}{\partial t} \tag{1}$$

where ϕ is the porosity of reservoir rocks, ρ_f is the fluid density, $\mathbf{v}$ is the Darcy's velocity vector, Q_f is a mass source term, α is the Biot coefficient, and ε_V is the volumetric strain. This means that variations of fluid content in time (first term) are balanced by the fluid flow (second term), additional fluid sources (first term on the righthand side), and volumetric change of the pore space (second term on the righthand side). The increase of volumetric strain causes the increase of the volume fraction to accommodate fluids, and acts as a liquid sink.

Considering the porosity and density as functions of fluid pore pressure p, the first term can be re-arranged to take the form of a storage model:

$$\frac{\partial}{\partial t}\left(\rho_f \phi\right) = \rho_f S \frac{\partial p}{\partial t} \tag{2}$$

where the storage coefficient S is the change in fluid content ζ owing to fluid pore pressure changes under constant volumetric strain, given as $S = \partial\zeta/\partial p$. The poroelastic storage coefficient is expressed using the weighted compressibility of reservoir rocks κ_s and fluids κ_f:

$$S = \phi\kappa_f + (1-\alpha)(\alpha-\phi)\kappa_s \tag{3}$$

Neglecting inertial and viscous effects, Darcy's law for fluid-saturated reservoir rocks is given by:

$$\mathbf{v} = -\frac{k}{\mu}\left(\nabla p + \rho_f \mathbf{g}\right) \tag{4}$$

where k is the permeability of reservoir rocks, μ is the dynamic viscosity of fluids, and $\mathbf{g}$ is the gravity acceleration.

Combining equations (1)-(4) produces the governing equation of the fluid flow model:

$$\rho_f S \frac{\partial p}{\partial t} + \nabla\cdot\rho_f\left[-\frac{k}{\mu}\left(\nabla p + \rho_f \mathbf{g}\right)\right] = Q_f - \rho_f \alpha \frac{\partial \varepsilon_V}{\partial t} \tag{5}$$

3.2. Heat transfer between fluids and reservoir

The heat exchange within reservoir rocks filled with mobile fluids is described by the heat balance equation:

$$\left[(1-\phi)\rho_s C_{p,s} + \phi\rho_f C_{p,f}\right]\frac{\partial T}{\partial t} + \rho_f C_{p,f}\mathbf{v}\cdot\nabla T + \nabla\cdot\mathbf{q} = Q_h \tag{6}$$

where T is the temperature, Q_h is the heat source term, ρ_s is the rock density, and $C_{p,s}$ and $C_{p,f}$ are specific heat capacities for rocks and fluids at constant pressure, respectively. This suggests that variations of heat in time (first term) are balanced by the convection driven by the Darcy's velocity field (second term), thermal conduction (third term), and additional volumetric heat sources (righthand-sided term).

The conductive heat flux $\mathbf{q}$ is proportional to the temperature gradient, according to Fourier's law:

$$\mathbf{q} = -k_{eff}\nabla T \tag{7}$$

where k_{eff} is the effective thermal conductivity.

Convection plays a predominant role in transporting heat in fractured rocks, whilst thermal conduction limited within the rock matrix has a minor contribution (Rathnaweera et al., 2020). Processes of fluid flow and heat transport in geothermal systems can be accurately
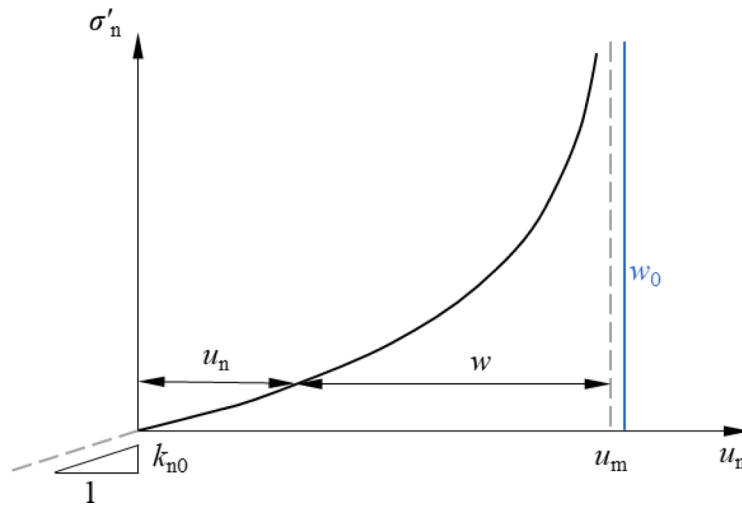
Figure 3. The hyperbolic relationship between fracture normal closure u_n and effective compressive stress σ'_n.

described by a dual-porosity model composed of two overlapping domains, one for matrix and pore space (primary porosity), and the other for solids and voids representing fractures (secondary porosity) (Gerke and Van Genuchten, 1993; Heinze and Hamidi, 2017). The dual-porosity model is appropriate to reflect the local thermal non-equilibrium in geothermal systems, as the instantaneous local thermal equilibrium may not be fully applicable owing to the temperature gradient between matrix and fractures (Gelet et al., 2013). However, the use of this model is largely limited as it becomes computationally cumbersome for large-scale models. As an alternative, a single-porosity (effective thermal conductivity) model treating pore space and fractures as one continuum can be employed to represent conduction for fractured rocks (Heinze and Hamidi, 2017). The single-porosity model is simple and fast to implement, and has sufficient accuracy when local thermal equilibrium can be reached rapidly.

Due to the high computational cost associated with the large model scale, the single-porosity model was used in this work. This model may not fully represent the relatively slow heat transfer from rock matrix to fractures, and cause local overestimation of thermal effects within the rock matrix. Nevertheless, as rocks at the Hellisheiði geothermal field are known to be extensively fractured, this would not cause a large influence on the THM behaviour of field-scale fractured rocks, which is the focus of this work.

3.3. Geomechanical deformation

The mechanical deformation of reservoir rocks is based on stress equilibrium described by the linear momentum balance equation, which is written as:

$$\nabla \cdot \sigma + \mathbf{F} = 0 \tag{8}$$

where σ is the total stress tensor, and $\boldsymbol{F}$ is the body force vector.

The total strain in reservoir rocks includes the thermoporoelastic strain caused by the thermoporoelastic stress (the first term), and stress-free strain induced by both pore pressure and temperature changes (the second and third terms) (Cao et al., 2022):

$$\varepsilon = \frac{1}{2G}\left(\sigma - \frac{\nu}{1+\nu}tr\sigma\right) + \frac{\alpha}{3K}p\mathbf{I} + \alpha_T \Delta T\mathbf{I} \tag{9}$$

where G and ν are the shear modulus and Poisson's ratio of reservoir rocks, respectively, α_T is the thermal expansion coefficient of reservoir rocks, and K is the bulk modulus of reservoir rocks. $\boldsymbol{\varepsilon}$ is the total strain tensor given as $\varepsilon = (\mathbf{u}\nabla + \nabla\mathbf{u})/2$, where $\boldsymbol{u}$ is the displacement vector. $tr\sigma$ is the trace of the total stress tensor (i.e., the summation of three

orthogonal longitudinal stresses), and $\boldsymbol{I}$ is the unit tensor. p is the fluid pressure, and ΔT is the temperature change.

The minimum principal strain ε_3 in the Húsmúli area (oriented in the fault-normal direction) is of particular interest. According to Equation (9), this can be expressed as:

$$\varepsilon_3 = -\frac{\nu}{E}\sigma_1 - \frac{\nu}{E}\sigma_2 + \frac{1}{E}\sigma_3 + \frac{\alpha}{3K}p + \alpha_T\Delta T \tag{10}$$

where E is the Young's modulus of reservoir rocks, and σ_1, σ_2 and σ_3 are the three principal stresses.

Equation (9) can be re-arranged to yield the expression for total stress:

$$\sigma = 2G\left(\varepsilon + \frac{\nu}{1-2\nu}\varepsilon_V\mathbf{I}\right) - \alpha p\mathbf{I} - 3K\alpha_T\Delta T\mathbf{I} \tag{11}$$

where ε_V is the volumetric strain given as $\varepsilon_V = \nabla \cdot \mathbf{u}$. The effective stress tensor $\boldsymbol{\sigma}'$ is defined by:

$$\sigma' = \sigma + \alpha p\mathbf{I} \tag{12}$$

In addition to a mechanical component generated due to constraints imposed by boundary confinement to oppose the deformation (effective stress change, first term in Equation (11)), the total stress (or the thermoporoelastic stress) also includes a poro component caused by the pore pressure change to drive volumetric dilation/contraction under unconstrained stress states (second term), and a thermal component caused by the temperature change under unconstrained stress states (third term). Reservoir rocks are subjected to in-situ thermoporoelastic stresses due to the initial fluid pressure and temperature. The poroelastic and thermoelastic stressing discussed in this work represent poroelastic and thermoelastic stress changes caused by fluid pressure and temperature changes, respectively.

3.4. Stress-dependent permeability

Representing the influence of geomechanics on permeability changes is essential for accurate simulation of hydrological behaviour in geothermal reservoirs. Previous efforts in characterisation of flow paths at the Hellisheiði geothermal field incorporated an experimentally-derived stress-dependent permeability relationship, which led to significant improvements in history matching results of tracer tests (Mahzari et al., 2021). This work implemented a physics-based stress-dependent permeability model for fractured rocks in the geothermal reservoir, representing the influence of fracture aperture change caused by both normal closure and tensile opening subjected to fluid injection and transient cooling conditions.
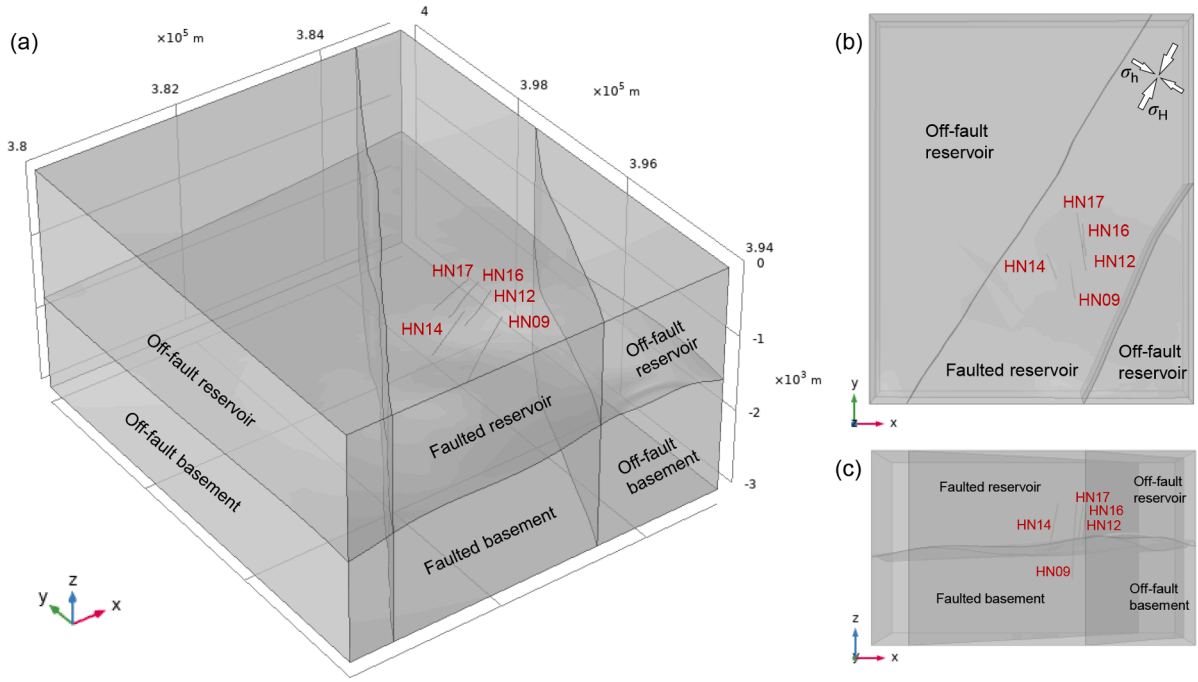
Figure 4. 3D geometry of the coupled THM model for fluids re-injection to five wells at the Húsmúli area: (a) 3D view, (b) plan view, and (c) side view. Coordinates of the model geometry follow the ISN93 geographic coordinate system suitable for use in Iceland.

The permeability of a model element containing conductive fractures oriented parallel to fault planes is represented by a lumped permeability k_b considering contribution from both rock matrix and fractures:

$$k_b = k_m + k_f \tag{13}$$

where k_m is the matrix permeability, and k_f is the effective fracture permeability. Owing to the small deformation of rock matrix, the lumped permeability is considered to come entirely from the effective fracture permeability for fractured rocks in the neighbourhood of fault structures at the Hellisheiði geothermal field.

Assuming that fractures have equal aperture for simplicity, the effective fracture permeability k_f for a model element hosting a number of parallel conductive fractures is given by (Witherspoon et al., 1980):

$$k_f = \frac{n_f w^3}{12l} \tag{14}$$

where w is the fracture aperture, l is the model element size, and n_f ($= f_d l$, f_d being the conductive fracture density) is the number of conductive fractures.

An individual fracture may experience either normal closure or tensile opening depending on the prevailing stress state (positive for compression) (Cao et al., 2021c, 2021b):

$$w = \begin{cases} w_0 + u_t, & \sigma'_n < 0 \\ w_0 - u_n, & \sigma'_n \geq 0 \end{cases} \tag{15}$$

where w_0 is the fracture aperture under unstressed conditions, and u_n and u_t are changes in fracture aperture due to normal closure and tensile opening, respectively.

Under compressive stress conditions, the change in fracture aperture is described by a hyperbolic relationship with the effective normal stress σ'_n (Bandis et al., 1983):

$$u_n = \frac{\sigma'_n u_m}{k_{n0} u_m + \sigma'_n} \tag{16}$$

where u_n is the normal fracture closure, u_m is the maximum allowable closure, and k_{n0} is the initial normal stiffness of fractures. As illustrated

in Figure 3, a fracture becomes more difficult to close owing to increasing normal stiffness under increasing effective normal stress. The maximum allowable fracture normal closure u_m is bounded by the fracture aperture under unstressed conditions w_0:

$$u_m \approx w_0 = w + u_n \tag{17}$$

Under tensile stress conditions, the increment in fracture aperture accounts for the incremental tensile strain Δe_t in the fracture-normal direction in host rocks, neglecting the small deformation of rock matrix. Therefore, the relative change in fracture aperture due to tensile opening can be expressed by the relative change in fracture porosity of host rocks:

$$\frac{u_t}{w_i} = \frac{\Delta \phi_f}{\phi_f} = \frac{\Delta e_t}{f_d w_i} \tag{18}$$

where w_i is the fracture aperture at in-situ stress, and ϕ_f and $\Delta \phi_f$ are the fracture porosity and change in fracture porosity, respectively.

Substituting Equations (15)-(18) to (14), the variation in the effective fracture permeability k_f caused by normal closure or tensile opening of fractures is given by:

$$\frac{k_f}{k_{fi}} = \begin{cases} \left(\dfrac{w_0}{w_i} + \dfrac{\Delta e_t}{f_d w_i} \right)^3, & \sigma'_n < 0 \\[3mm] \left[\dfrac{k_{n0} u_m^2}{(\sigma'_n + k_{n0} u_m) w_i} \right]^3, & \sigma'_n \geq 0 \end{cases} \tag{19}$$

where k_{fi} is the effective fracture permeability at in-situ stress. The permeability of faulted rocks at any effective normal stress state can be derived from only three parameters, i.e., the initial effective fracture permeability k_{fi}, initial normal stiffness of fractures k_{n0}, and fracture porosity ϕ_f. Other parameters can be computed from the three parameters: the in-situ fracture aperture w_i and fracture density f_d are dependent on the in-situ effective fracture permeability k_{fi} and fracture porosity ϕ_f, and the maximum allowable fracture closures w_0 (u_m) is determined according to the hyperbolic fracture normal closure model.

A similar stress-dependent permeability model was implemented to simulate permeability changes of fractured rocks in Drift-Scale Heater

Table 1

Material properties used in the coupled THM model. Initial value for stress-dependent faulted reservoir permeability at 1,000 m depth in bold.

Parameters	Hyalocalstic formation (faulted)	Hyalocalstic formation (off-fault)	Basalt basement	References
Physical and mechanical properties				
Density ρ (kg/m^3)	2,700	2,700	2,700	
Young's modulus E (GPa)	25	60	60	Juncu et al. (2020)
Poisson's ratio υ	0.25	0.25	0.25	Juncu et al. (2020)
Hydrological properties				
Porosity ϕ (%)	10	10	8.09	Stefánsson et al. (1997), Snæbjörnsdóttir (2014)
Initial permeability (mD)	**30**	15	3.75	Stefánsson et al. (1997), Snæbjörnsdóttir (2018, 2014)
Biot coefficient α	1	1	1	
Thermodynamic properties				
Heat capacity C_p (J/kg/K)	1,000	1,000	1,000	Tómasdóttir (2018)
Thermal conductivity k_s (W/m/K)	2.1	2.1	2.1	Tómasdóttir (2018)
Coefficient of thermal expansion α_T (1/K)	2×10^{-5}	2×10^{-5}	2×10^{-5}	Juncu et al. (2017)
Fracture properties				
Initial effective fracture permeability k_{fi} (mD)	**30**	-	-	
Fracture density f_d (m^{-1})	18.6	-	-	
Initial normal stiffness k_{n0} (GPa/m)	50	-	-	
Fracture porosity ϕ_f (%)	0.05	-	-	
Initial fracture aperture w_i (mm)	0.027	-	-	
Maximum allowable closure u_m (mm)	0.063	-	-	

Tests in a coupled thermo-mechanical (TM) model of the proposed Yucca Mountain repository (Hsiung et al., 2005), and in CO$_2$ geological storage applications in a coupled hydro-mechanical (HM) model of the In Salah storage site (Cao et al., 2021c), both satisfactorily validated against field measurements. The stress-dependent permeability model implemented in this work was verified against the analytical solution of effective fracture permeability for a set of parallel persistent conductive fractures, as shown in Appendix A.

## 4. Coupled THM modelling of geothermal fluids injection at Hellisheiði

4.1. Model set-up

As shown in Figure 4, a 3D coupled THM model of the Húsmúli re-injection area measuring 5 km × 6 km × 3 km (easting × northing × depth) was constructed in COMSOL Multiphysics to model the spent fluids re-injection process into the five injection wells and the thermo-hydrological-mechanical behaviour of the geothermal reservoir over a 1-year period. The lithology and geological structures of the coupled model was constructed based on a geological model of the Húsmúli re-injection area, which comprises surface mapping data, geophysics data, well data, well logging data, laboratory analyses data (Gunnarsdóttir and Poux, 2016). The geology of the area was simplified to two stratigraphical layers, the hyalocalstic reservoir formation (mostly above 1,600 m depth) and basalt bedrock (mostly below 1,600 m depth). The five fault structures (F1-F5) and surrounding regions within 200 m distance were modelled as faulted regions comprised of fractured rocks. The areal extent of faulted regions was determined based on observations that the majority of induced seismicity recorded at Húsmúli tend to fall within 200 m distance to the five major fault structures (Cao et al., 2021a). The secondary fracture systems were neglected in order to reduce the complexity of meshing and high computational costs for the 3D coupled model. Following the geological model, the faulted regions were extended to the ground surface to match the surface fault map, and down to 3,000 m depth to allow fluid flow at varying depths.

The five injection wells were implemented in the model following realistic well trajectories. The open borehole sections for HN09, HN12, HN14, HN16 and HN17 extend from 800 m to depths of 2499.1 m, 1476.7 m, 1547.3 m, 1625.0 m and 1501.8 m, respectively. Except for HN09, which has a lower section in the basalt bedrock, all the other

wells are restricted within the reservoir domain. The injection wellbore diameter is 0.3 m. Instead of fully resolving wells as cylindrical surfaces, the injection wells were modelled using the well feature, which provides accurate model solutions with significantly simplified meshing. Refined triangular meshes with a maximum element size of 30 m were created for the injection wells. The remaining domain was discretised by a free tetrahedral mesh with a maximum element size of 300 m, which becomes progressively coarser away from the wells.

Both the reservoir and bedrock formations were assumed to have uniform mechanical, hydrological and thermodynamic properties. The linear elastic constitutive model was used to model the geomechanical response of the reservoir to fluid injection. The off-fault reservoir and basalt basement were assigned with the same elastic properties, while the Young's modulus E of the faulted reservoir was assumed to be degraded to 40% of its original value. The Young's modulus E of the faulted reservoir used in the model was 25 GPa, the upper bound estimated through interpretation of geodetic data based on a Poisson's ratio $\upsilon = 0.25$ (Juncu et al., 2020). Based on experimental analyses on 80 samples of basaltic hyalocalstic tuffs (Frolova et al., 2004; Snæbjörnsdóttir et al., 2014), the reservoir formation was considered to exhibit broad variations in both porosity and permeability, falling within the range of 0.14-0.57 and 0.001-6,400 mD, respectively. In the reservoir modelling work of Snæbjörnsdóttir et al. (2018), the faulted reservoir was assigned with a porosity of 0.10 and a permeability of 30 mD, and the basalt bedrock a porosity of 0.08 and a permeability of 3.75 mD. Porosity and permeability values used in this model followed their work, except that the permeability for the faulted reservoir domain was determined through matching the field measured injectivity for the five injection wells over a 1-year re-injection period. The initial permeability value calibrated for the faulted reservoir domain was 30 mD at 1,000 m reservoir depth in this model. According to the stress-dependent permeability relationship using this initial permeability, the permeabilities at the top and bottom of the faulted reservoir domain are 200 mD and 15 mD, respectively, which are in general within the range for the reservoir permeability. The off-fault reservoir domains were assigned with a lower permeability of 15 mD. Mechanical, hydrological and thermodynamic parameters used for both the reservoir and bedrock, along with data sources wherever available, are presented in Table 1. A compressibility κ_f of 4.5×10^{-10} Pa^{-1} was used for water at high temperature and pressure conditions (Fine and Millero, 1973). Temperature-dependent values were used for other hydrological and
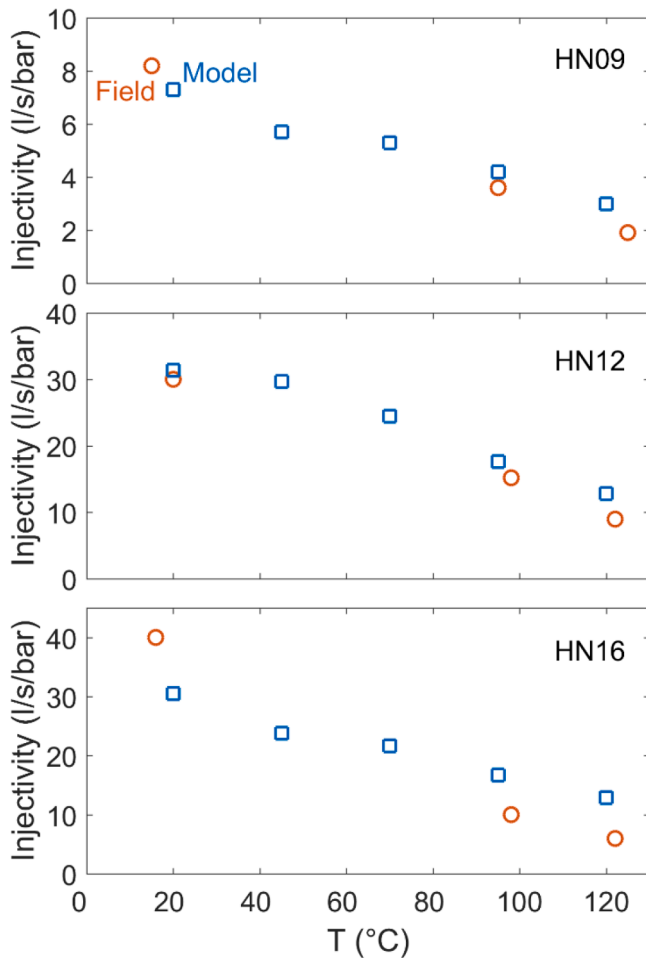
Figure 5. Comparison between field measured injectivity (Gunnarsson, 2013) and model derived values in this study for different temperatures of re-injected water in three wells at the Húsmúli area. The field measured injectivity for wells HN-12 and HN-16 were not well defined at 20 °C.

thermodynamic parameters of re-injected water, involving density, dynamic viscosity, thermal conductivity and heat capacity.

The orientation and magnitude of the in-situ stress field at the Húsmúli area were estimated based on borehole breakouts and tensile fracture observation from resistivity image logs (Batir, 2011). The maximum in-situ horizontal principal stress is oriented 22.5° off the north direction. The gradient for the vertical stress σ_v is 29.5 MPa/km, and those for the maximum and minimum horizontal stresses σ_H and σ_h are constrained in the range of 71.3–76.0 and 13.0–29.5 MPa/km, respectively. The minimum values for both σ_H and σ_h within the range were used in this model. The stress field in the model was initialised by applying on model boundaries respective normal and shear stress components of the in-situ stress, considering a 200 m overburden. Following on from Equation (9), the initial strain caused by both pore pressure and thermal expansion was also assigned to the model to ensure a uniform in-situ stress distribution at the same depth. The boundary conditions of the model were set in such a way that normal and shear stresses computed from the horizontal stress gradients were applied to lateral boundaries and the base was fixed.

The natural groundwater table is around 200 m above the sea level at the Húsmúli area, resulting in a 20 bar overpressure (Gunnarsson, 2013). The in-situ fluid pressure was vertically distributed based on gravitational equilibrium using a water density of 1,000 kg/m³, in additional to the overpressure throughout the model. All the outer boundaries were assigned as fluid pressure boundaries matching the initial fluid pore pressure distribution.

The temperature was initialised based on a vertical thermal gradient of 0.2 K/m (Snæbjörnsdóttir et al., 2014) and a temperature of 10°C in the top layer. All the outer boundaries were set as temperature boundaries with the same thermal gradient to ensure initial equilibrium.

4.2. Modelling and seismicity potential evaluation procedure

The 3D coupled model constructed was first calibrated in terms of hydrological behaviour across broad temperature ranges (see Section 4.3). The calibrated model was then used to simulate fluids re-injection to the five injection wells and the associated thermo-hydrological-mechanical behaviour at the Húsmúli area over a 1-year re-injection period. Re-injection operations were modelled in such a way that the wellhead pressure was controlled at 8 bar and temperature of re-injected fluids at 70 °C in all the five injection wells. In order to identify the respective contribution from different mechanisms for induced seismicity, three coupled model scenarios were considered:

(1) Model Scenario 1 (under poroelastic effect): Thermal and mechanical coupling components are switched off, so that the heat transfer process is separately modelled, without contributing to the expansion/contraction of reservoir rocks. This model scenario represents only the effect of elevated fluid pore pressure and poroelastic stressing on the stress field.

(2) Model Scenario 2 (under thermoporoelastic effect): The thermal expansion/contraction effect is further considered in addition to Model Scenario 1. This model scenario represents the effect of elevated fluid pore pressure, poroelastic stressing and thermoelastic stressing on the stress field.

(3) Model Scenario 3 (under thermoporoelastic effect with permeability enhancement): The fluid injection and transient cooling-induced permeability enhancement is further considered in addition to Model Scenario 2. This model scenario represents the effect of elevated fluid pore pressure, poroelastic stressing, thermoelastic stressing and permeability enhancement on the stress field, and thus is the model scenario most representative of realistic field conditions.

To facilitate comparison between model scenarios, the stress-dependent permeability model was activated for the faulted reservoir domain in all the three model scenarios, with the permeability during model runs being fixed (permeability being related to the virgin stress field) in Model Scenarios 1 and 2, but being allowed to vary with prevailing stresses in Model Scenario 3. To investigate the thermal influence of re-injected fluids, a set of model runs for Model Scenario 3 were further examined by varying the temperature of re-injected fluids from 20 °C to 120 °C with an interval of 25 °C. The built-in MUMPS direct solver was used to solve the model, employing the backward differentiation formulas (BDF) method for time stepping.

The thermo-hydrological-mechanical behaviour of the geothermal reservoir in response to fluid re-injection in the models was analysed and compared. Based on coupled model results, the potential for seismicity was further evaluated in terms of Coulomb failure stress changes ΔCFS, defined as the static stress change caused by the co-seismic fracture slippage:

$$\Delta CFS = \Delta\tau - f(\Delta\sigma - \Delta p) \qquad (20)$$

where f is the friction coefficient along the fracture plane, and $\Delta\tau$ and $\Delta\sigma$ are changes in shear and normal stresses resolved on the fracture plane, respectively (positive for compression) (Cao et al., 2020; Cao et al., 2021c; Scholz, 2002). A positive ΔCFS indicates an enhancement of the potential for fractures slippage, and a negative ΔCFS suggests an inhibition. The potential for seismicity was only examined along the fault-trending direction (22.5°) in this work. The friction coefficient μ used in the evaluation was 0.6.
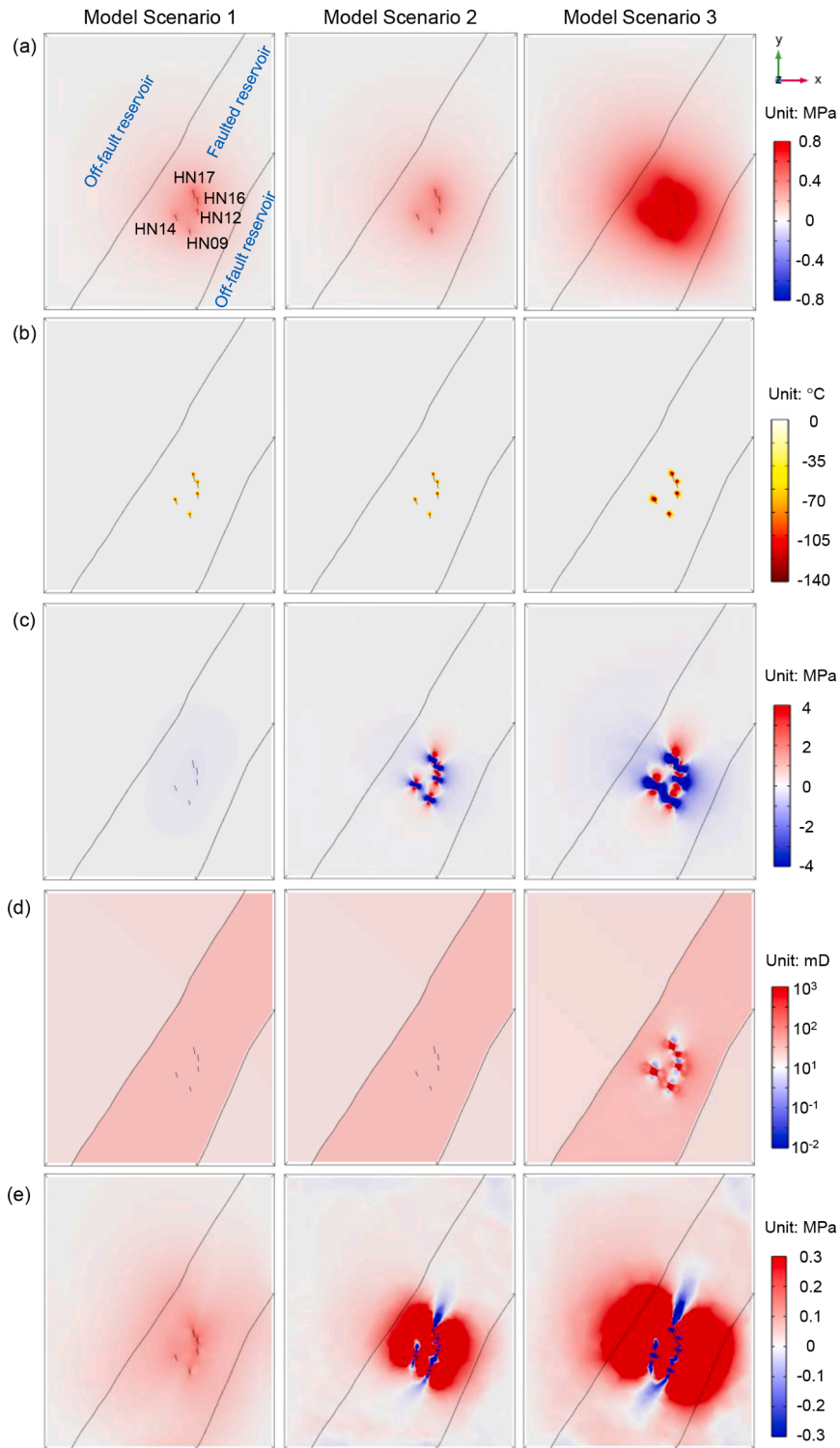
Figure 6. Geomechanical and hydrological behaviour at 1,000 m depth after 1-year of fluid injection at the Húsmúli area for the three model scenarios: (a) pore pressure change Δp, (b) temperature change ΔT, (c) minimum effective principal stress change $\Delta \sigma'_3$, (d) permeability k, and (e) Coulomb failure stress change ΔCFS.

4.3. Model calibration

To accurately represent the transient cooling-induced permeability enhancement at different temperatures of re-injected fluids, the coupled model was first calibrated through matching model derived injectivity values from Model Scenario 3 with field measured values in an injectivity test. The injectivity test was carried out for three injection wells (HN09, HN12 and HN16) before the Húsmúli area was commissioned

for re-injection in September 2011 (Gunnarsson, 2013). The field measured injectivity of HN12 and HN16 are not very accurate at the lowest temperature because the wells became so permeable that the pressure changes were not clear during the pumping tests. As shown in Figure 5, the injectivity is increased by around 4 times when cooling re-rejected fluids from 120°C down to 20°C in all the three injection wells. Compared to other injection wells, HN09 has a considerably lower injectivity in that only HN09 has a lower borehole section into the
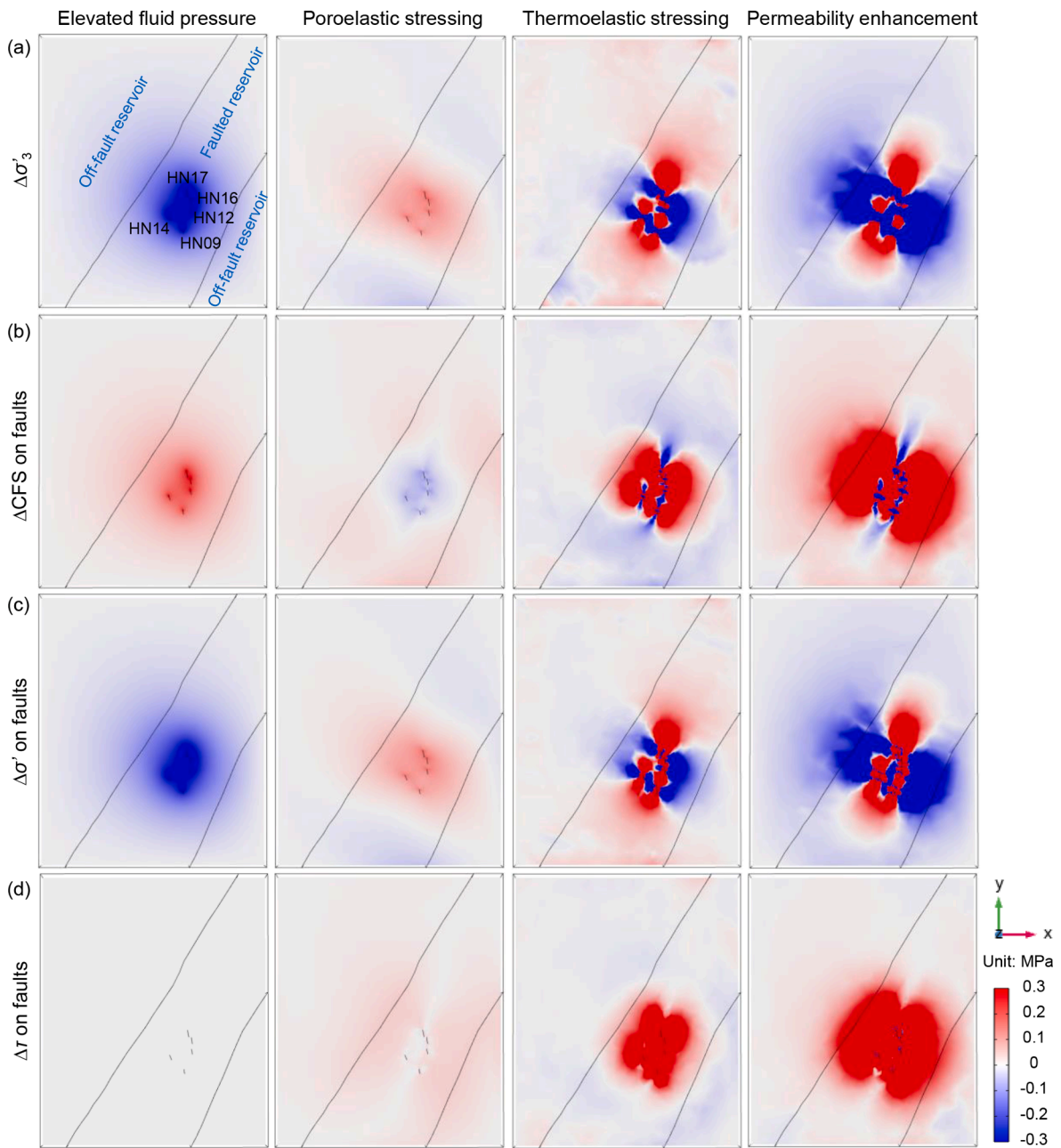
Figure 7. (a) Minimum effective principal stress change $\Delta\sigma'_3$, and (b) Coulomb failure stress change ΔCFS, (c) change of effective normal stress on preferably oriented faults $\Delta\sigma'$, and (d) change of shear stress along preferably oriented faults $\Delta\tau$ at 1,000 m depth after 1-year of fluid injection at the Húsmúli area contributed by four individual mechanisms (elevated fluid pressure, poroelastic stressing, thermoelastic stressing and permeability enhancement).

reservoir basement with a much lower permeability, and thus has a lower average fluid mass flow rate.

The injectivity at the Hellisheiði geothermal field is predominantly contributed by fracture permeability. According to Poiseuille's law for laminar flow through a fracture, the injectivity is proportional to $\frac{Q_i}{p} = \frac{Ww^3}{12\mu L}$, where W and L are the fracture width and length, respectively. Both the viscosity of fluids μ and fracture aperture w vary as a function of temperature. The viscosity of water μ is about five times higher at 20°C than at 120°C, indicating a positive correlation between the injectivity and temperature. The completely opposite correlation in field observations suggests that the fracture aperture w has a counteractive yet overwhelming effect on the injectivity. The thermoelastic stress change caused by re-injection of cold fluids causes contraction of rock matrix, leading to an increase of the fracture aperture w. The effects of both the

viscosity of water μ and fracture aperture w were considered in the coupled THM model. The first was considered by built-in temperature-dependent material properties in the solver, and the latter by implementation of the stress-dependent permeability model for the faulted reservoir domain.

Model calibration was performed to reproduce the field injectivity behaviour not only at a temperature of re-injected fluids at 70 °C, but also across the full spectrum of possible temperatures. This means that the calibrated model realistically represents the coupled THM process, and thus could be used to 1) identify the dominant mechanism for induced seismicity, and 2) examine the temperature dependence of mechanisms for induced seismicity. During model calibration, a number of modelling trials were run by tuning three hydrological and fracture parameters, i.e., the initial effective fracture permeability k_{fi}, initial normal stiffness k_{n0}, and fracture porosity ϕ_f of the faulted reservoir. It

was found that the injectivity at a fixed temperature of re-injected fluids could be effectively controlled through adjusting the three parameters, but the extent of relative change in injectivity at different temperatures is insensitive to them. This is because well injectivity is associated with hydromechanical behaviour (governed by calibrated hydrological and fracture parameters), while temperature dependence of the injectivity is a result of thermal expansion of the rock matrix (governed by given thermodynamic parameters).

As presented in Figure 5, using the set of material properties presented in Table 1 the model is able to capture the inverse correlation between temperature and injectivity, and achieve fairly good agreement with field measured values for all the three injection wells. But, the temperature dependence of injectivity predicted by the model is slightly less appreciable than what is observed in field measured values across the temperature range of interest. This is believed to be because the transient cooling-induced tensile failure and associated stress transfer around the injection wells were not considered in the model, which leads to an underestimation of the volume of enhanced permeability around the injection wells at lower temperatures. Therefore, the calibrated model may be considered to represent the lower bound of the temperature effect and can be used to evaluate the key physics occurring in the coupled system.

5. Model results and analysis

5.1. THM behaviour and potential for enhanced seismicity

Figure 6 presents thermo-hydro-mechanical behaviour and potential for seismicity at 1,000 m depth after 1-year of fluid injection at the Húsmúli area for the three model scenarios. When only the poroelastic effect is considered (Model Scenario 1), overpressurised regions extend slightly beyond the faulted reservoir (Figure 6a, first column). In comparison, transient cooling regions have a much smaller extent and are only concentrated around the injection wells due to slow thermal convection and conduction (Figure 6b, first column). Both the minimum effective principal stress and Coulomb failure stress changes $\Delta\sigma'_3$ and ΔCFS are caused by combined effects of fluid pore pressure increase and poroelastic stressing, and mostly concentrated around the injection wells (Figure 6e, first column). Farther away from the injection wells, stress perturbations also form as a result of the contrast in poroelastic response in regions characterised by nonuniform pore pressure distribution and heterogeneous elastic properties (bulk modulus and Poisson's ratio), according to Equation (9).

When the thermoporoelastic effect is considered (Model Scenario 2), both overpressurised regions and transient cooling regions are barely influenced (Figure 6a and b, second column). Compared to pore pressure change and poroelastic stressing, transient cooling has an overwhelming influence on the minimum effective principal stress $\Delta\sigma'_3$. It results in significant rock contraction and stress relaxation immediately surrounding the injection wells (coloured in blue in Figure 6c, second column); consequently, stress concentration is also formed around the stress relieved regions along the fault-parallel direction (coloured in red in Figure 6c, second column). Considering that the in-situ minimum effective principal stress is ~4 MPa at 1,000 m depth, it is anticipated that rocks surrounding the injection wells change from compressive to tensile stress states (coloured in dark blue) and are likely to be subjected to tensile failure extending the thermoelastic effect further away (which is not modelled in this work). The distribution of Coulomb failure stress change ΔCFS exhibits a two-lobed pattern, with much elevated magnitudes in the faulted reservoir (Figure 6e, second column). There is also localised suppression of the potential for seismicity in stress concentration regions (in Figure 6c, second column), where the increased normal effective stress inhibits the potential of fracture slippage.

When the fluid injection and transient cooling-induced permeability enhancement is further considered (Model Scenario 3), the areal extent of permeability enhanced regions can reach over 300 m away from the injection wells, with the permeability around the injection wells being enhanced by over two orders of magnitude (Figure 6d, third column). As a result of enhanced fluids flow and thus heat transfer, both the overpressurised and transient cooling regions expand extensively, as compared to the previous two model scenarios (Figure 6a and b). The minimum effective principal stress relaxation regions increase as well, with the area of tensile stress regions more than doubled (Figure 6c). The extent of the enhanced potential of seismicity is enlarged significantly beyond the faulted reservoir, and most of the planar model domain is characterised by a positive Coulomb failure stress change (Figure 6e).

For the four mechanisms considered (i.e., elevated fluid pressure, poroelastic stressing, thermoelastic stressing and transient cooling-induced permeability enhancement), Model Scenario 1 represents the effects of the first two on the geomechanical and reservoir behaviour, Model Scenario 2 the effects of the first three, and Model Scenario 3 the effects of all the four mechanisms. To identify the dominant mechanism accounting for induced seismicity, Figure 7 presents the respective contribution from each individual mechanism to the minimum effective principal stress change $\Delta\sigma'_3$ and Coulomb failure stress changes ΔCFS. The elevated fluid pressure effect and poroelastic effect can be respectively represented by the poro and mechanical components of the total stress obtained from Model Scenario 1. Stress components relevant to the thermoelastic effect and enhanced permeability effect cannot be directly separated from those relevant to the poroelastic effect, as changes in poro and thermal components would lead to a change in the mechanical component at confined stress conditions. Here, the thermoelastic effect is isolated by taking the difference of results between Model Scenarios 2 and 1, and the enhanced permeability effect by taking the difference of results between Model Scenarios 3 and 2. As the fault strike is aligned with in-situ principal stress directions, the effective normal stress change $\Delta\sigma'$ on preferably oriented faults, even if subjected to fluid injection and transient cooling, approximates to the minimum effective principal stress change $\Delta\sigma'_3$ (Figure 7a and c). Therefore, only the effects of the four mechanisms on the effective normal stress change on preferably oriented faults $\Delta\sigma'$ are presented.

Pore pressure change reduces the effective normal stress on preferably oriented faults $\Delta\sigma'$ by the same amount but does not change the shear stress $\Delta\tau$, resulting in an increase of the Coulomb failure stress change ΔCFS (Figure 7 b, c and d, first column). Under an increased pore pressure, reservoir rocks under confinement respond in a manner that the bulk expansion is opposed by increased compressive stress of a lesser amount within the overpressurised region, and decreased compressive stress of a lesser amount surrounding the region (coloured in red and blue respectively in Figure 7c, second column). While the poroelastic response of homogeneous reservoir rocks under uniform pore pressure only involves bulk expansion but not shear deformation, Equation (9) suggest that shear stress is induced in regions where there is either a pore pressure gradient (up to several hundreds of metres away from the injection wells) or a contrast of elastic properties (near contacts of faulted and off-fault reservoir sections) (Figure 7d, second column). With contribution from both the normal effective stress change $\Delta\sigma'$ and shear stress change $\Delta\tau$, the poroelastic stressing reduces the potential for seismicity within the overpressurised region but enhances the potential surrounding the region (Figure 7b, second column). The combined effects of pore pressure change and poroelastic stressing on the Coulomb failure stress change ΔCFS, represent overall favourable conditions for the potential for seismicity, as shown in Model Scenario 1 in Figure 6e (first column).

The thermoelastic effect leads to compressive stress relaxation around the injection wells in the fault-normal direction, and concentration in the fault-parallel direction (Figure 7c, third column). Analogous to the poroelastic effect, the thermoelastic effect only results in bulk expansion/contraction but not shear deformation for homogeneous reservoir rocks subjected to uniform temperature change (Equation (9)). However, shear stress is generated where there is a thermal gradient (Figure 7d, third column). As opposed to that caused by the poroelastic
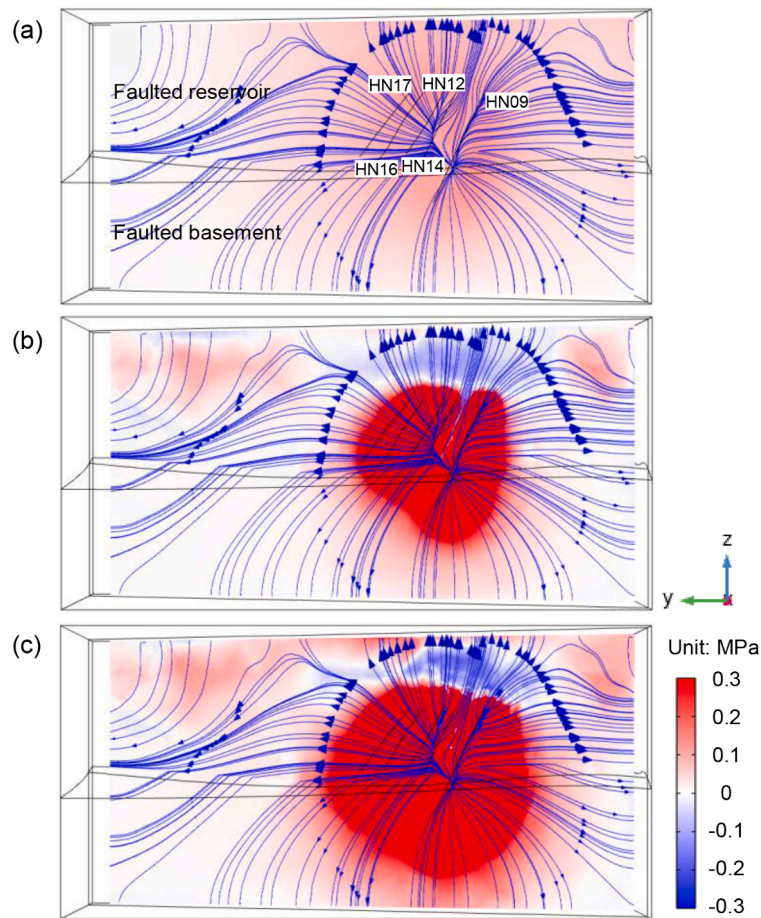
Figure 8. Coulomb failure stress change ΔCFS along Fault F3 after 1-year of fluid injection at the Húsmúli area for the three model scenarios: (a) Model Scenario 1, (b) Model Scenario 2, and (c) Model Scenario 3. The Darcy's velocity field is illustrated by blue arrowed streamlines.

effect, positive shear stress change $\Delta\tau$ caused by the thermoelastic effect concentrates much closer around the injection wells, owing to the smaller area of the transient cooling region in comparison to the over-pressurised region. With contribution from both effective normal stress change $\Delta\sigma'$ and shear stress change $\Delta\tau$, the thermoelastic effect enhances the potential for seismicity within the two lobes, and suppresses outside them (Figure 7b, third column). It is worth mentioning that the favourable effects of pore pressure change and poroelastic stressing on the potential for seismicity could overwhelm the thermoelastic-induced inhibition outside the two-lobed region, and the combined effects of pore pressure change, poroelastic stressing and thermoelastic stressing represent an overall enhanced potential for seismicity (Figure 6e, second column).

Fluid injection and transient cooling-induced permeability enhancement facilitates both fluid flow and heat transfer, and intensifies all the first three mechanisms by accelerating changes in pore pressure, temperature, and normal effective stress and shear stress on preferably oriented faults (Figure 7, fourth column). Under enhanced permeability, the physical thermo-hydro-mechanical coupling process remains the same, so as the spatial pattern of the Coulomb failure stress change ΔCFS, but the magnitude of ΔCFS is increased significantly (Figure 6, second and third columns). While the combined effects of the four mechanisms account for the full thermo-hydro-mechanical behaviour of geothermal reservoirs, the fluid injection and transient cooling-induced permeability enhancement exerts the dominant control through significantly enhancing the first three mechanisms.

To help evaluate the potential for induced seismicity at different depths (in particular within the reservoir basement), Figure 8 presents the comparison between ΔCFSs calculated along the vertical fault F3

from the three model scenarios. As illustrated by arrowed streamlines, fluids flowing into the reservoir basement are significantly slowed down owing to its relatively lower permeability. Nevertheless, over-pressurisation is still sustained within the reservoir basement, representing an overall enhanced potential for seismicity across the fault section (Figure 8a). Although the thermoelastic effect and the permeability enhancement effect barely influence the Darcy's velocity field, they can play a significant role towards enhanced potential for seismicity across the fault section through thermal convection. It is noted that a region with suppressed potential for seismicity (coloured in blue) forms above the region with enhanced seismic potential (coloured in red) in Figure 8b and c. This is because the reservoir above the injection level is subjected to thermoelastic effects of colder re-injected spent fluids and hotter in-situ geothermal fluids, both carried upwards by the Darcy's velocity field. When colder re-injected fluids gradually get heated through thermal convection while flowing upwards, the thermoelastic effect of hotter in-situ geothermal fluids prevails and results in suppressed potential for seismicity.

5.2. Temperature dependence of THM behaviour and potential for enhanced seismicity

Figure 9 presents the thermo-hydro-mechanical behaviour and potential for seismicity after 1-year of fluid injection at the Húsmúli area for different temperatures of re-injected fluids in Model Scenario 3. Notably, overpressurised regions, transient cooling regions, tensile stress regions, permeability enhanced regions and regions with enhanced potential for seismicity expand by several times in area when the temperature of re-injected fluids is reduced from 120°C to 20°C. In
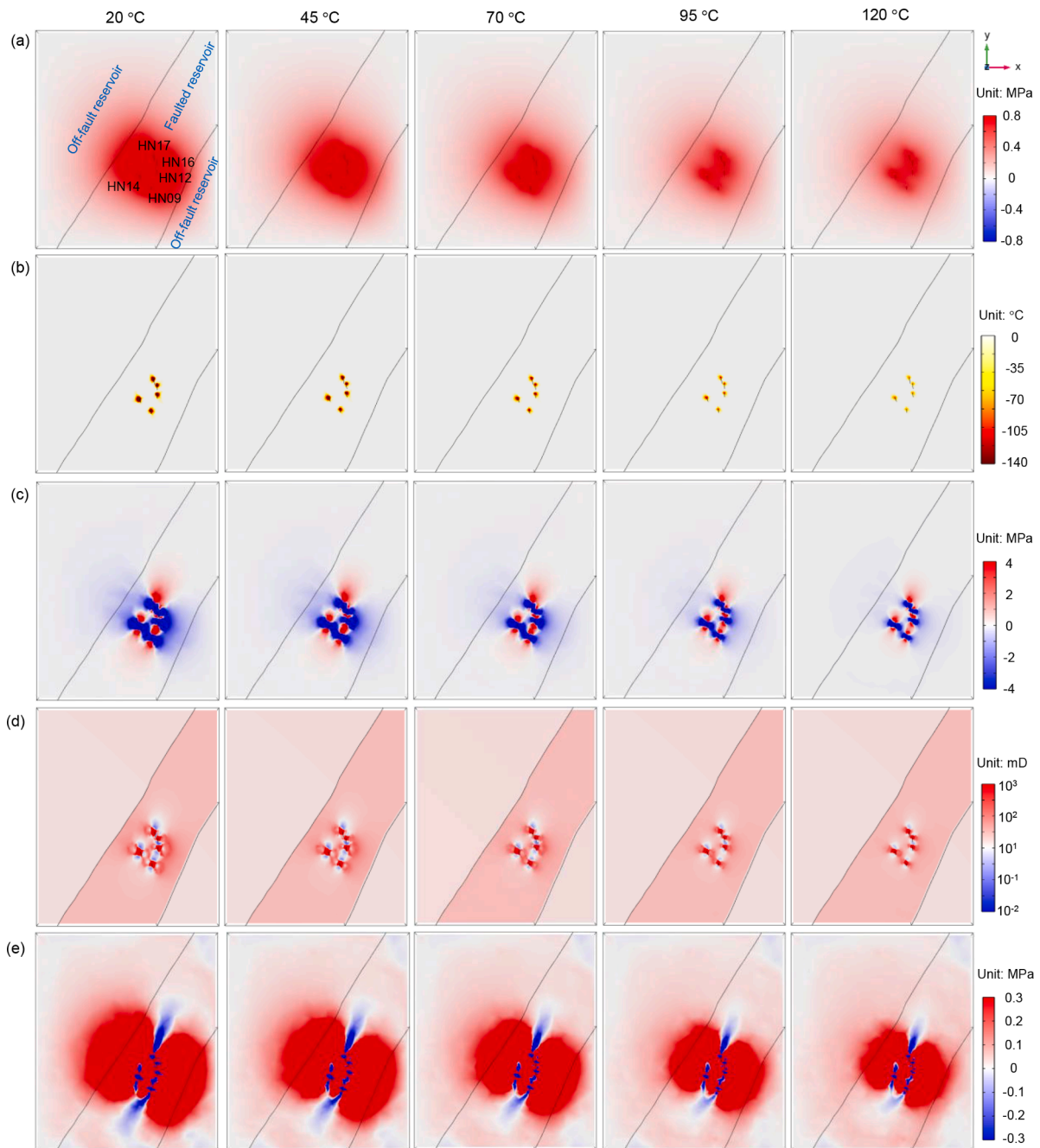
Figure 9. Geomechanical and hydrological behaviour at 1,000 m depth after 1-year of fluid injection at the Húsmúli area for different temperatures of re-injected fluids in Model Scenario 3: (a) pore pressure change Δp, (b) temperature change ΔT, (c) minimum effective principal stress change $\Delta\sigma'_3$, (d) permeability k, and (e) Coulomb failure stress change ΔCFS.

particular, regions with enhanced potential for seismicity extend well beyond the faulted reservoir at a fluid re-injection temperature of 20°C, as opposed to being restricted within the faulted reservoir at 120°C, which explains the temperature-dependent induced seismicity observed at the Hellisheiði geothermal field.

Depending upon the specific coupling between multiphysics, the thermoelastic effect, the transient cooling-induced permeability enhancement effect, or their compound effects account for the temperature dependence of each individual thermal, hydrological and mechanical behaviour. The pore pressure change Δp is merely relevant to the permeability enhancement. Driven by the Darcy's velocity field, the temperature change ΔT is influenced by not only temperature variations but also permeability enhancement. Both the minimum effective

principal stress change $\Delta\sigma'_3$ and Coulomb failure stress change ΔCFS are attributed to the combined action of thermoelastic effect and permeability enhancement.

6. Discussion

6.1. Comparison between recorded seismicity and model results

Seismicity recorded at the Húsmúli area during September 2011 – April 2012 (Gunnarsson, 2013) were used to compare with the model results. As shown in Figure 10, seismicity data are grouped by depth (1, 750 m $\pm$ 250 m, 2,250 m $\pm$ 250 m, and 2,750 m $\pm$ 250 m) and plotted against Coulomb failure stress change contours at the respective depths
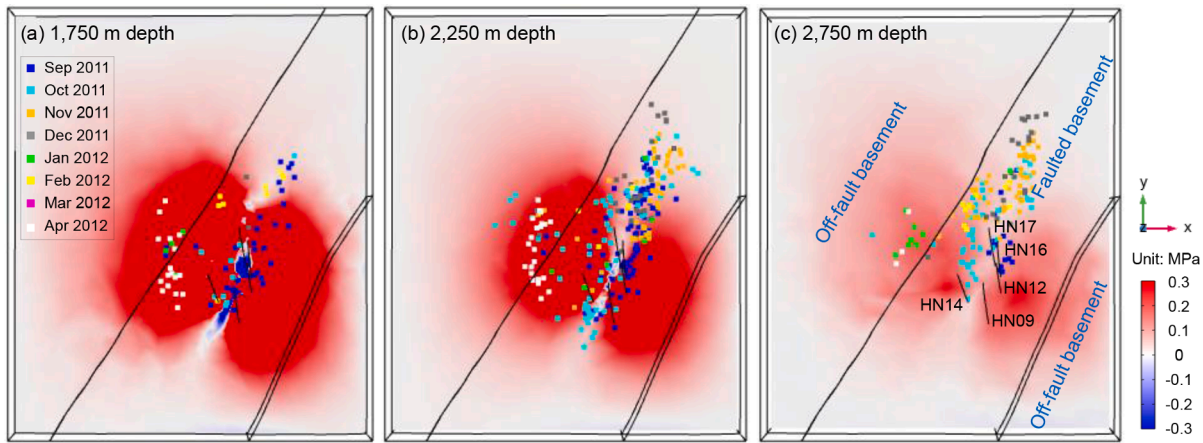
Figure 10. Comparison between recorded seismicity and modelled Coulomb failure stress change ΔCFS after 1-year of fluid injection at the Húsmúli area (Model Scenario 3, re-injected fluids temperature 70 °C): (a) recorded seismicity at depths 1,750 m ± 250 m superimposed on ΔCFS contour at depth 1,750 m, (b) recorded seismicity at depths 2,250 m ± 250 m superimposed on ΔCFS contour at depth 2,250 m, (c) recorded seismicity at depths 2,750 m ± 250 m superimposed of ΔCFS contour at depth 2,750 m.
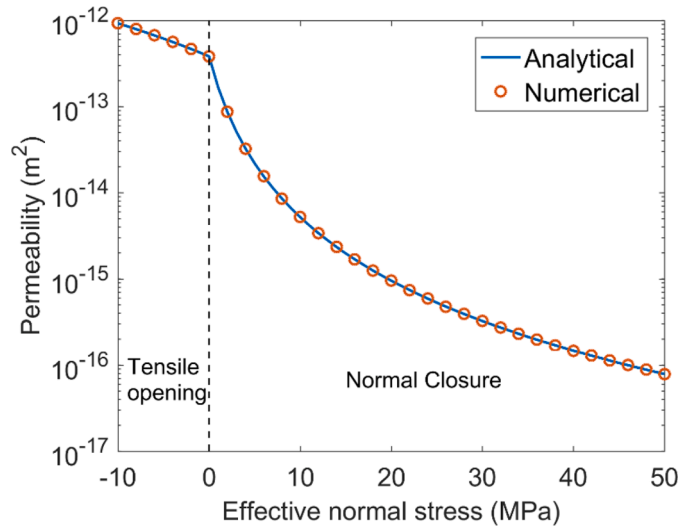
Figure A1. Verification of the stress-dependent permeability model implemented against the analytical solution for a set of persistent conductive fractures under both compressive and tensile stress conditions.

calculated from Model Scenario 3. The spatial distribution of Coulomb failure stress changes at greater depths are similar to those presented in Figure 6e, third column, while the values for stress changes decrease with depth. The spatial distribution of recorded seismicity is generally consistent with the region with enhanced potential for seismicity from the model. As shown in each sub-figure, seismicity recorded at the three depth intervals form two clusters, one in immediate neighbourhood of the injection wells and trending to the strike of pre-existing faults, and the other falling within the left lobe of the region with enhanced potential. At each depth interval, the first seismic cluster formed shortly after the onset of re-injection operations in September 2011, followed by extension along the faults as fluid conduits. The second seismic cluster did not form until January 2012, and grew into shape in April 2012. The temporal evolution of seismicity reflects the fluid flow process, which promotes not only pore pressure change, but also temperature change and cooling-induced permeability enhancement of reservoir rocks.

It is worth mentioning that few recorded seismicity falls within the right lobe estimated to have enhanced potential for seismicity. This is believed to be because the nearly uniform Darcy's velocity field formed within the faulted reservoir in the current model may not fully represent

the complex structural geology and preferential fluid flow paths at the geothermal field Khodayar et al. (2015). carried out outcrop fracture mapping using aerial imagery at the Húsmúli area, and identified three major fracture systems, trending to NE-ENE, WNW and NS directions. These fracture systems intersect the major fault structures, and are predominantly located to the west of the injection wells. Tracer tests carried out in 2013 – 2015 suggested that re-injected fluids flow from the wells to the north and northwest, but the flow to the southeast is inhibited (Kristjánsson et al., 2016). In addition, there are a number of production wells at least 500 m to the east of the injection wells, and geothermal fluids production (which was not modelled in this work) may lower the prevailing pore pressure to the east of the injection wells, not only influencing the fluid flow and heat transfer, but also having a counteractive effect on the potential for induced seismicity. Nevertheless, these do not undermine the confidence that the current model has successfully captured essential physical mechanisms underlying the induced seismicity. The recent work of Mahzari et al. (2021) used the mapped fracture systems to infer preferential fluid flow paths through matching tracer test profiles at the Hellisheiði geothermal field, which provides the basis to improve the current model by honouring physical constraints much better.

The spatial distribution of recorded seismicity compares most favourably with results of Model Scenario 3 amongst the three model scenarios. This indicates that all four mechanisms considered are at play in triggering seismicity at the Húsmúli area. The thermoporoelastic effect without transient cooling-induced permeability enhancement may not explain the full set of seismicity recorded, as the region with enhanced potential for seismicity from the model is restricted to the faulted reservoir section even at 1,000 m depth after 1-year of fluid re-injection (Figure 6e). The general agreement between the seismic locations and the two-lobed pattern indicates that the thermoelastic stressing and transient cooling-induced permeability enhancement are the governing mechanisms for induced seismicity at the Hellisheiði geothermal field.

Juncu et al. (2020) proposed two elastic half-space models, Model A with a single source (a steeply dipping opening fault) and Model B with two sources (a spherical pressure source and a strike-slip fault), to fit the injection-induced surface deformation at the Hellisheiði geothermal field. They found no correlation between Coulomb failure stress changes calculated for Model A and seismicity recorded between September 2011 and May 2012, and concluded that elevated pore pressure and the associated fault opening are unlikely to account for the seismicity recorded. The pressure source of a 1.1 km radius in their Model B covers the most volume around recorded seismicity, and thus provides a

plausible explanation for their occurrence. However, the spherical pressure source selected is at 2.7 km depth, with its centre located around 500 m north of the injection wells. This may not be realistic considering that the increased pore pressure emanates from the injection wells at reservoir intervals (around 800 – 1,500 m depth). In contrast, the alternative mechanisms for induced seismicity provided in this work appear to be more convincing in that they satisfactorily match field observations while respecting the physical process and constraints.

Hypocentres of the majority of seismicity recorded are located in the basalt bedrock at depths between 1,500 - 2,500 m, with much lower stress perturbations than at reservoir intervals. It is thus hypothesised that hyalocalstic reservoir rocks are characterised by stronger mechanical properties and more stable, whilst basaltic basement rocks are weaker and susceptible to fracture slippage. Another plausible reason might be that faults in the hyalocalstic formation are more in favour of aseismic slip, and that the difference in lithology accounts for the aseismic/seismic slip transition.

6.2. Comparison between poroelastic stressing, thermoelastic stressing and permeability enhancement

The occurrence of induced seismicity is described by the Mohr-Coulomb slippage criterion, where a fracture plane is deemed to slip when the shear stress along the plane τ exceeds the resistance to slip, which is the product of the friction coefficient f and the effective normal stress $(\sigma - p)$. As such, any effect that influences one or more of the terms involved may be considered as an individual mechanism. Amongst the four mechanisms examined, fluid overpressure modifies p, poroelastic stressing alters σ, thermoelastic stressing relates to both σ and τ, and transient cooling-induced permeability enhancement changes both σ and τ through the change of p. It is noteworthy that both the latter two mechanisms can be referred to as thermal effects, but they should be distinguished from each other. The thermoelastic stressing is direct TM coupling that operates through interactions between mechanical and thermal fields, whereas the permeability enhancement is indirect THM coupling that modifies mechanical or hydraulic properties due to stress/pressure changes and thus affects the stress/pressure fields (Rutqvist and Stephansson, 2003).

The poroelastic stressing effect can be represented by changes in the poro component and the mechanical component of the total stress in Equation (11). In geothermal fluids re-injection, the increase in pore pressure tends to expand rocks but is resisted by the elastic response of rocks, resulting in an increase in the poroelastic stress but a decrease in the effective stress (less compressive; Figure 6a, first column). Analogically, the thermoelastic stressing effect can be represented by changes in the thermal component and the mechanical component of the total stress in Equation (11). In re-injection of cold fluids, the decrease in temperature tends to contract rocks but is opposed by the elastic response of rocks, leading to a decrease in the thermoelastic stress and also a decrease in the effective stress (less compressive or become tensile; Figure 6c, second column). The permeability enhancement effect can be represented by changes in poro, thermal, and mechanical component of the total stress in Equation (11). The transient-cooling induced permeability enhancement associated with geothermal fluids re-injection facilitates both the exchange of fluids and heat in the reservoir, and thus both poroelastic and thermoelastic stressing effects.

Under unconstrained stress states, the ratio of contributions from thermoelastic and poroelastic stressing in geothermal exploitation can be quantified by (Segall and Fitzgerald, 1998):

$$\frac{\sigma^{thermo}}{\sigma^{poro}} = \frac{3K\alpha_T}{\alpha}\frac{\Delta T}{\Delta p} \tag{21}$$

For a Biot coefficient $\alpha = 1$, bulk modulus $K = 16.7$ GPa, and thermal expansion coefficient $\alpha_T = 2 \times 10^{-5}$ K^{-1} (as in Table 1), the coefficient term in the equation is 1 MPa/°C (a pore pressure of 1 MPa results in the same amount of stress change as a temperature change of 1°C). Provided that $\Delta p = 0.8$ MPa and $\Delta T = -190$ - -90°C (corresponding to temperatures of re-injected fluids ranging from $20 \sim 120$°C) around injection wells at 1,000 m depth at Hellisheiði, the ratio of thermoelastic to poroelastic stressing is within the range -237.5 - -112.5, indicating a dominating control of the thermoelastic stressing. When reservoir rocks are under confining stresses, the thermoelastic effect still plays the dominant role, with the ratio of thermoelastic to poroelastic stressing remaining the same order of magnitude (Figure 6c, first and second columns).

In geothermal fluids injection, both the pore pressure increase and temperature decrease are in favour of a decrease in the effective stress, bringing the Mohr stress circle of reservoirs towards the failure/slippage envelope. In comparison, the reduction in both pore pressure and temperature in geothermal production has counteractive effects on the effective stress. The thermoelastic effect may not be so pronounced during geothermal production owing to a modest temperature change in the reservoir. As an example, $\Delta T/\Delta p$ during production at the Geysers geothermal field is around 19°C/MPa at 3 MPa reservoir pressure, as estimated from the slope of the vapor-pressure curve (Segall and Fitzgerald, 1998). This corresponds to a ratio to thermoelastic to poroelastic stressing of 8 or more.

It is noted that the analysis and comparison referred to above are restricted to the immediate neighbourhood of the injection wells, where ΔT is the largest possible temperature decrease. Considering that transient cooling regions have more limited areal extent compared to overpressurised regions, the reduction in temperature is significantly lower in most of the reservoir over a 1-year re-injection period, so as the ratio of thermoelastic to poroelastic stressing. It is also worth mentioning that while pore pressure and temperature changes and most material properties are well constrained, the thermal expansion coefficient α_T of reservoir rocks are subjected to certain variability. The value used in the model is fairly reasonable for a rock with basalt-like composition (Juncu et al., 2017), but thermal expansion coefficient for other rock types may be as low as 5×10^{-6} K^{-1} (Segall and Fitzgerald, 1998). It is argued that, even for a thermal expansion coefficient at the lower end of the possible spectrum, the thermoelastic stress change generated still outweighs the poroelastic stress change under operational conditions at Hellisheiði.

Thermal effects (both direct temperature change and transient cooling-induced permeability enhancement) are closely associated with the amount of heat transferred from re-injected spent fluids, which can be quantified by $Q_f = C_p M_0 \Delta T$, where M_0 is the mass flow. The direct temperature change is represented by the temperature difference ΔT, while the permeability enhancement effect is proportional to the mass flow rate M_0. The temperature dependence of induced seismicity can be attributed to both the temperature difference ΔT and the mass flow M_0. The ratio between the change in magnitude of the two variables for different temperatures of re-injected fluids reflects the respective contribution of the thermoelastic effect and the transient cooling-induced permeability enhancement.

At the Hellisheiði geothermal field, the ratio of the temperature difference between re-injection at 20°C and 120°C is $190/90 = 2.1$ at 1,000 m depth. This ratio is larger at shallower depths and smaller at greater depths, depending on the prevailing temperature difference between re-injected fluids and the reservoir (e.g., 3.0 at 800 m depth, and 1.5 at 1,600 m depth). In contrast, the amount of mass flow rate M_0 is increased by around 4 times at the fixed injection pressure when reducing the temperature of re-injected fluids from 120°C to 20°C, due to the around 4-fold increase in injectivity. The estimation above supports that the transient-cooling induced permeability enhancement (a ratio of the amount of heat transferred of around 4) has a more significant influence than the thermoelastic effect alone (a ratio of the amount of heat transferred in the range of 1.5-3.0 at reservoir intervals). The total ratio of the amount of heat transferred between re-injection at 20°C and 120°C can be as large as 8.4 at 1,000 m depth, and this explains the

high sensitivity of induced seismicity to temperature.

During the period of investigation, the cooling contraction regions have more limited areal extent compared to overpressurised regions at the Hellisheiði geothermal field, due to the nature of fluid flow and heat transfer. However, it is anticipated that both the areal extent of cooling contraction and fluid overpressure would expand over time, but at different rates (Ghassemi and Tao, 2016; Izadi and Elsworth, 2015; Jeanne et al., 2014b). The pore pressure distribution and Darcy's velocity field are not expected to change significantly owing to the relatively large permeability of the faulted reservoir, whilst there would be a continuous temperature decrease in the neighbourhood of the injection wells, and transient cooling and thermoelastic stressing regions will continue to expand. Therefore, the thermal effects (both thermoelastic stress and permeability enhancement) would play a less pronounced role in reservoir-wide stress changes in a short-term time scale (i.e., several to several tens of days), but a more pronounced role in a long-term time scale (i.e., several tens of years). Future work may include extension of the current coupled THM model to simulate the geothermal exploitation on a longer time scale and evaluate the long-term potential for induced seismicity.

7. Conclusions

This paper presents the development of a 3D coupled THM model to simulate cold fluids re-injection process over a 1-year period and investigate the governing mechanism for induced seismicity at the Hellisheiði geothermal field. The coupled model developed could model fluid flow, heat transfer, geomechanics and stress-dependent permeability, which allows to disentangle the effects towards Coulomb stress changes from elevated fluid pore pressure, poroelastic stressing, thermoelastic stressing, and fluid injection and transient cooling-induced permeability enhancement. In particular, the contribution of the permeability enhancement as indirect THM coupling could be isolated from the thermoelastic stressing as direct TM coupling. The 3D coupled model was calibrated against field injectivity values based on field measurements, and regions with enhanced potential for seismicity were found to be fairly consistent with the spatial distribution of field monitored induced seismicity. The coupled model was also used to investigate the temperature dependence of induced seismicity associated with geothermal fluids re-injection.

Model findings have shown that induced seismicity associated with fluids re-injection at the geothermal field is under combined effects of pore pressure change, poroelastic stressing, thermoelastic stressing, and fluid injection and transient cooling-induced permeability enhancement. In the vicinity of injection wells, the contribution to Coulomb stress changes from the permeability enhancement effect is almost twice of that from the direct thermoelastic stressing, which is in turn two orders of magnitude larger than that from the poroelastic stressing. This indicates that the permeability enhancement effect is the dominant mechanism for induced seismicity at the Hellisheiði geothermal field.

By reducing temperature of re-injected fluids from 120°C to 20°C at the Hellisheiði geothermal field, the amount of heat transferred is increased by 8.4 times at 1,000 m depth, where the temperature change is increased by 2.1 times, and the amount of mass flow by around 4 times. This indicated that while the temperature dependence of field injectivity is governed by transient cooling-induced permeability enhancement, the temperature-dependence of induced seismicity is attributed to both direct thermoelastic effect (related to temperature change) and transient cooling-induced permeability enhancement (related to increased mass flow). The outcomes from this work have significant implications for the regulation of injection-induced seismic risk through temperature control of re-injected fluids in geothermal exploitation.

CRediT authorship contribution statement

Wenzhuo Cao: Conceptualization, Methodology, Software, Investigation, Writing – original draft. **Sevket Durucan:** Funding acquisition, Resources, Project administration, Writing – review & editing. **Ji-Quan Shi:** Methodology, Writing – review & editing. **Wu Cai:** Methodology, Writing – review & editing. **Anna Korre:** Funding acquisition, Resources, Project administration, Writing – review & editing. **Thomas Ratouis:** Resources, Writing – review & editing.

Declaration of Competing Interest

The authors declare that they have no known competing financial interests or personal relationships that could have appeared to influence the work reported in this paper.

Appendix A. Verification of the stress-dependent permeability model

The stress-dependent permeability model implemented in this work was verified against the analytical solution of effective fracture permeability (Equation (14)) under both compressive and tensile stress conditions. A 100 m × 100 m 2D model was constructed to represent a 1,000 m-deep horizontal plane across faulted reservoir rocks, assuming that faults are oriented in the x direction. The same set of material parameters for the fractured reservoir domain as presented in Table 1 was used. Lumped permeability values, equivalent to effective fracture permeability values for a set of parallel persistent conductive fractures comprising of the faults, were assigned to the model elements. Stresses applied on the lateral boundaries were 74.2 MPa (corresponding to the in-situ maximum effective horizontal principal stress at 1,000 m depth), and those on the top and bottom boundaries were varied between -10 MPa (tension) and 50 MPa (compression) at an interval of 2 MPa. The equivalent permeability of the faulted reservoir was measured through steady-state fluid flow simulations with a permeameter-type boundary condition, where a macroscopic pressure differential of 1 kPa was applied at two opposite lateral model boundaries whilst other boundaries were impervious.

As shown in Figure A1, permeability values measured from the numerical model achieve an excellent match with the analytical solution for the set of fractures at varying stress conditions. Note that the equivalent permeability at 4.2 MPa (the in-situ minimum effective horizontal stress at 1,000 m depth) is 30 mD, consistent with the initial permeability at 1,000 m depth presented in Table 1.

References

Ariki, K., Hatakeyama, K., 1997. Effects of the injection temperature on injectivity of geothermal wells. J. Geotherm. Res. Soc. Japan 19, 197–208.

Bandis, S.C., Lumsden, A.C., Barton, N.R., 1983. Fundamentals of rock joint deformation. Int. J. Rock Mech. Min. Sci. Geomech. Abstr. 20, 249–268.

Batir, J.F., 2011. Master's thesis. University of Iceland.

Benson, S.M., 1987. Analysis of thermally induced permeability enhancement in geothermal injection wells.

Blöcher, G., Cacace, M., Jacquey, A.B., Zang, A., Heidbach, O., Hofmann, H., Kluge, C., Zimmermann, G., 2018. Evaluating micro-seismic events triggered by reservoir

operations at the geothermal site of Groß Schönebeck (Germany). Rock Mech. Rock Eng. 51, 3265–3279.

Candela, T., Van Der Veer, E.F., Fokker, P.A., 2018. On the importance of thermo-elastic stressing in injection-induced earthquakes. Rock Mech. Rock Eng. 51, 3925–3936.

Cao, W., Durucan, S., Cai, W., Shi, J.-Q., Korre, A., Jamnikar, S., Rošer, J., Lurka, A., Siata, R., 2020. The role of mining intensity and pre-existing fracture attributes on spatial, temporal and magnitude characteristics of microseismicity in longwall coal mining. Rock Mech. Rock Eng. 53, 4139–4162.

Cao, W., Durucan, S., Cai, W., Shi, J.-Q., Korre, A., Ratouis, T., Hjörleifsdóttir, V., Sigfússon, B., 2021a. Combining microseismic observations and reservoir simulation to interpret fracture criticality in faults at the Hellisheidi geothermal field, Iceland. In: 55th US Rock Mechanics/Geomechanics Symposium. American Rock Mechanics Association, pp. 1–10.

Cao, W., Lei, Q., Cai, W., 2021b. Stress-dependent deformation and permeability of a fractured coal subject to excavation-related loading paths. Rock Mech. Rock Eng 1–22 https://doi.org/https://doi.org/10.1007/s00603-021-02520-0.

Cao, W., Shi, J.-Q., Durucan, S., Korre, A., 2021c. Evaluation of shear slip stress transfer mechanism for induced microseismicity at In Salah CO2 storage site. Int. J. Greenh. Gas Control 107.

Cao, W., Verdon, J.P., Tao, M., 2022. Coupled Poroelastic Modeling of Hydraulic Fracturing-Induced Seismicity: Implications for Understanding the Post Shut-In ML 2.9 Earthquake at the Preston New Road, UK. J. Geophys. Res. Solid Earth, 10.1029/2021JB023376.

De Simone, S., Vilarrasa, V., Carrera, J., Alcolea, A., Meier, P., 2013. Thermal coupling may control mechanical stability of geothermal reservoirs during cold water injection. Phys. Chem. Earth, Parts A/B/C 64, 117–126.

Eyinla, D.S., Oladunjoye, M.A., 2021. Controls of fault geometry and thermal stress on fault slip modes: Implications for permeability enhancement and injection-induced seismicity. Pet. Res.

Fine, R.A., Millero, F.J., 1973. Compressibility of water as a function of temperature and pressure. J. Chem. Phys. 59, 5529–5536.

Frolova, J., Franzson, H., Ladygin, V., Sigurdsson, O., Stefánsson, V., Shustrov, V., 2004. Porosity and permeability of hyaloclastites tuffs, Iceland. In: Proceedings of International Geothermal Workshop IGW2004 "Heat and Light from the Heart of the Earth, pp. 9–16.

Fuchs, S.J., Crandall, D., Moore, J.E., Sivaguru, M., Fouke, B.W., Espinoza, D.N., Akono, A.-T., Werth, C.J., 2021. Geochemically induced shear slip in artificially fractured dolomite-and clay-cemented sandstone. Int. J. Greenh. Gas Control 111, 103448.

Gan, Q., Elsworth, D., 2014a. Analysis of fluid injection-induced fault reactivation and seismic slip in geothermal reservoirs. J. Geophys. Res. Solid Earth 119, 3340–3353.

Gan, Q., Elsworth, D., 2014b. Thermal drawdown and late-stage seismic-slip fault reactivation in enhanced geothermal reservoirs. J. Geophys. Res. Solid Earth 119, 8936–8949.

Gan, Q., Lei, Q., 2020. Induced fault reactivation by thermal perturbation in enhanced geothermal systems. Geothermics 86, 101814.

Gelet, R., Loret, B., Khalili, N., 2013. Thermal recovery from a fractured medium in local thermal non-equilibrium. Int. J. Numer. Anal. Methods Geomech. 37, 2471–2501.

Gerke, H.H., Van Genuchten, M.T., 1993. A dual-porosity model for simulating the preferential movement of water and solutes in structured porous media. Water Resour. Res. 29, 305–319.

Ghassemi, A., Kumar, G.S., 2007. Changes in fracture aperture and fluid pressure due to thermal stress and silica dissolution/precipitation induced by heat extraction from subsurface rocks. Geothermics 36, 115–140.

Ghassemi, A., Nygren, A., Cheng, A., 2008. Effects of heat extraction on fracture aperture: A poro–thermoelastic analysis. Geothermics 37, 525–539.

Ghassemi, A., Tao, Q., 2016. Thermo-poroelastic effects on reservoir seismicity and permeability change. Geothermics 63, 210–224.

Ghassemi, A., Zhou, X., 2011. A three-dimensional thermo-poroelastic model for fracture response to injection/extraction in enhanced geothermal systems. Geothermics 40, 39–49.

Grigoli, F., Cesca, S., Rinaldi, A.P., Manconi, A., Lopez-Comino, J.A., Clinton, J.F., Westaway, R., Cauzzi, C., Dahm, T., Wiemer, S., 2018. The November 2017 Mw 5.5 Pohang earthquake: A possible case of induced seismicity in South Korea. Science (80-.) 360, 1003–1006.

Gunnarsdóttir, S.H., Poux, B., 2016. 3D Modelling of Hellisheiði Geothermal Field using Leapfrog: Data, Workflow and Preliminary Models. Report ÍSOR-2016.

Gunnarsson, G., 2013. Temperature Dependent Injectivity and Induced Seismicity–Managing Reinjection in the Hellisheiði Field. SW-Iceland. GRC Trans. 37, 1019–1025.

Heinze, T., Hamidi, S., 2017. Heat transfer and parameterization in local thermal non-equilibrium for dual porosity continua. Appl. Therm. Eng. 114, 645–652.

Hodneland, E., Gasda, S., Kaufmann, R., Bekkvik, T.C., Hermanrud, C., Midtømme, K., 2019. Effect of temperature and concentration of impurities in the fluid stream on CO2 migration in the Utsira formation. Int. J. Greenh. Gas Control 83, 20–28.

Hsiung, S.M., Chowdhury, A.H., Nataraja, M.S., 2005. Numerical simulation of thermal–mechanical processes observed at the Drift-Scale Heater Test at Yucca Mountain, Nevada, USA. Int. J. Rock Mech. Min. Sci. 42, 652–666.

Izadi, G., Elsworth, D., 2015. The influence of thermal-hydraulic-mechanical-and chemical effects on the evolution of permeability, seismicity and heat production in geothermal systems. Geothermics 53, 385–395.

Jeanne, P., Rutqvist, J., Dobson, P.F., Walters, M., Hartline, C., Garcia, J., 2014a. The impacts of mechanical stress transfers caused by hydromechanical and thermal processes on fault stability during hydraulic stimulation in a deep geothermal reservoir. Int. J. Rock Mech. Min. Sci. 72, 149–163.

Jeanne, P., Rutqvist, J., Hartline, C., Garcia, J., Dobson, P.F., Walters, M., 2014b. Reservoir structure and properties from geomechanical modeling and microseismicity analyses associated with an enhanced geothermal system at The Geysers. California. Geothermics 51, 460–469.

Ji, Y., Hofmann, H., Duan, K., Zang, A., 2022. Laboratory experiments on fault behavior towards better understanding of injection-induced seismicity in geoenergy systems. Earth-Science Rev, 103916.

Ji, Y., Wu, W., 2020. Injection-driven fracture instability in granite: Mechanism and implications. Tectonophysics 791, 228572.

Juncu, D., Árnadóttir, T., Geirsson, H., Guðmundsson, G.B., Lund, B., Gunnarsson, G., Hooper, A., Hreinsdottir, S., Michalczewska, K., 2020. Injection-induced surface deformation and seismicity at the Hellisheidi geothermal field, Iceland. J. Volcanol. Geotherm. Res. 391, 106337.

Juncu, D., Árnadóttir, T., Hooper, A., Gunnarsson, G., 2017. Anthropogenic and natural ground deformation in the Hengill geothermal area, Iceland. J. Geophys. Res. Solid Earth 122, 692–709.

Kang, F., Li, Y., Huang, X., Li, T., 2022. Competition between cooling contraction and fluid overpressure on aperture evolution in a geothermal system. Renew. Energy.

Khodayar, M., Axelsson, G., Steingrímsson, B., 2015. Potential Structural Flow Paths for Tracers and Source Faults of Earthquakes at Húsmúli, Hengill, South Iceland, in: Technical Report 2015/035. ÍSOR.

Koh, J., Roshan, H., Rahman, S.S., 2011. A numerical study on the long term thermo-poroelastic effects of cold water injection into naturally fractured geothermal reservoirs. Comput. Geotech. 38, 669–682.

Kristjánsson, B.R., Axelsson, G., Gunnarsson, G., Gunnarsson, I., Óskarsson, F., 2016. Comprehensive tracer testing in the Hellisheidi Geothermal Field in SW-Iceland. In: Proceedings, 41st Workshop on Geothermal Reservoir Engineering.

Lee, Y.S., Kim, K.H., Lee, T.H., Sung, W.M., Park, Y.C., Lee, J.H., 2009. Analysis of CO2 endpoint relative permeability and injectivity by change in pressure, temperature, and phase in saline aquifer. Energy Sources, Part A Recover. Util. Environ. Eff. 32, 83–99.

Mahzari, P., Stanton-Yonge, A., Sanchez-Roa, C., Saldi, G., Mitchell, T., Oelkers, E.H., Hjorleifsdottir, V., Snaebjornsdottir, S.O., Ratouis, T., Striolo, A., 2021. Characterizing fluid flow paths in the Hellisheidi geothermal field using detailed fault mapping and stress-dependent permeability. Geothermics 94, 102107.

Majer, E.L., Baria, R., Stark, M., Oates, S., Bommer, J., Smith, B., Asanuma, H., 2007. Induced seismicity associated with enhanced geothermal systems. Geothermics 36, 185–222.

Megies, T., Wassermann, J., 2014. Microseismicity observed at a non-pressure-stimulated geothermal power plant. Geothermics 52, 36–49.

Pandey, S.N., Chaudhuri, A., Kelkar, S., 2017. A coupled thermo-hydro-mechanical modeling of fracture aperture alteration and reservoir deformation during heat extraction from a geothermal reservoir. Geothermics 65, 17–31.

Parisio, F., Vilarrasa, V., Wang, W., Kolditz, O., Nagel, T., 2019. The risks of long-term re-injection in supercritical geothermal systems. Nat. Commun. 10, 1–11.

Pollack, A., Horne, R., Mukerji, T., 2020. What are the challenges in developing Enhanced Geothermal Systems (EGS)? Observations from 64 EGS sites. In: Proceedings World Geothermal Congress. Reykjavik, Iceland, pp. 1–17.

Rangriz Shokri, A., Chalaturnyk, R.J., Nickel, E., 2019. Non-Isothermal Injectivity Considerations for Effective Geological Storage of CO2 at the Aquistore Site. In: SPE Annual Technical Conference and Exhibition. Society of Petroleum Engineers, Saskatchewan, Canada.

Rathnaweera, T.D., Wu, W., Ji, Y., Gamage, R.P., 2020. Understanding injection-induced seismicity in enhanced geothermal systems: From the coupled thermo-hydro-mechanical-chemical process to anthropogenic earthquake prediction. Earth-Science Rev, 103182.

Rutqvist, J., Rinaldi, A.P., Cappa, F., Jeanne, P., Mazzoldi, A., Urpi, L., Guglielmi, Y., Vilarrasa, V., 2016. Fault activation and induced seismicity in geological carbon storage – Lessons learned from recent modeling studies. J. Rock Mech. Geotech. Eng. 8, 789–804. https://doi.org/10.1016/j.jrmge.2016.09.001.

Rutqvist, J., Stephansson, O., 2003. The role of hydromechanical coupling in fractured rock engineering. Hydrogeol. J. 11, 7–40. https://doi.org/10.1007/s10040-002-0241-5.

Safari, R., Ghassemi, A., 2015. 3D thermo-poroelastic analysis of fracture network deformation and induced micro-seismicity in enhanced geothermal systems. Geothermics 58, 1–14.

Scholz, C.H., 2002. The Mechanics of Earthquakes and Faulting. Cambridge University Press.

Schultz, R., Skoumal, R.J., Brudzinski, M.R., Eaton, D., Baptie, B., Ellsworth, W., 2020. Hydraulic fracturing-induced seismicity. Rev. Geophys. 58, e2019RG000695.

Segall, P., Fitzgerald, S.D., 1998. A note on induced stress changes in hydrocarbon and geothermal reservoirs. Tectonophysics 289, 117–128.

Si, G., Cai, W., Wang, S., Li, X., 2020. Prediction of relatively high-energy seismic events using spatial–temporal parametrisation of mining-induced seismicity. Rock Mech. Rock Eng. 1–22.

Snæbjörnsdóttir, S.Ó., Tómasdóttir, S., Sigfússon, B., Aradóttir, E.S., Gunnarsson, G., Niemi, A., Basirat, F., Dessirier, B., Gíslason, S.R., Oelkers, E.H., 2018. The geology and hydrology of the CarbFix2 site, SW-Iceland. Energy Procedia 146, 146–157.

Snæbjörnsdóttir, S.Ó., Wiese, F., Fridriksson, T., Ármansson, H., Einarsson, G.M., Gislason, S.R., 2014. CO2 storage potential of basaltic rocks in Iceland and the oceanic ridges. Energy Procedia 63, 4585–4600.

Stefánsson, V., Sigurðsson, Ó., Guðmundsson, Á., Franzson, H., Friðleifsson, G.Ó., Tulinius, H., 1997. Core measurements and geothermal modelling. In: Second Nordic Symposium on Petrophysics, pp. 199–220.

Sun, C., Zhuang, L., Jung, S., Lee, J., Yoon, J.S., 2021. Thermally induced slip of a single sawcut granite fracture under biaxial loading. Geomech. Geophys. Geo-Energy Geo-Resources 7, 1–13.

Tawiah, P., Duer, J., Bryant, S.L., Larter, S., O`Brien, S., Dong, M., 2020. CO2 injectivity behaviour under non-isothermal conditions–Field observations and assessments from the Quest CCS operation. Int. J. Greenh. Gas Control 92, 102843.

Tómasdóttir, S., 2018. Flow Paths in the Húsmúli Reinjection Zone. Iceland.

Vilarrasa, V., Rinaldi, A.P., Rutqvist, J., 2017. Long-term thermal effects on injectivity evolution during CO2 storage. Int. J. Greenh. Gas Control 64, 314–322.

Weingarten, M., Ge, S., Godt, J.W., Bekins, B.A., Rubinstein, J.L., 2015. High-rate injection is associated with the increase in US mid-continent seismicity. Science (80- .) 348, 1336–1340.

Witherspoon, P.A., Wang, J.S.Y., Iwai, K., Gale, J.E., 1980. Validity of cubic law for fluid flow in a deformable rock fracture. Water Resour. Res. 16, 1016–1024.

Yao, J., Zhang, X., Sun, Z., Huang, Z., Liu, J., Li, Y., Xin, Y., Yan, X., Liu, W., 2018. Numerical simulation of the heat extraction in 3D-EGS with thermal-hydraulic-mechanical coupling method based on discrete fractures model. Geothermics 74, 19–34.

Ye, Z., Ghassemi, A., 2018. Injection-induced shear slip and permeability enhancement in granite fractures. J. Geophys. Res. Solid Earth 123, 9009–9032.

Zhou, X.X., Ghassemi, A., Cheng, A., 2009. A three-dimensional integral equation model for calculating poro-and thermoelastic stresses induced by cold water injection into a geothermal reservoir. Int. J. Numer. Anal. Methods Geomech. 33, 1613–1640.